Doppler synthetic aperture hitchhiker imaging

2010 Inverse Problems 26 065006

(http://iopscience.iop.org/0266-5611/26/6/065006)

Inverse Problems **26** (2010) 065006 (26pp) doi:10.1088/0266-5611/26/6/065006

Doppler synthetic aperture hitchhiker imaging

Can Evren Yarman[1], **Ling Wang**[2] **and Birsen Yazıcı**[3]

[1] Houston Technology Center, WesternGeco Schlumberger, Houston, TX 77042, USA
[2] College of Information Science and Technology, Nanjing University of Aeronautics and Astronautics, Nanjing, 210016, People's Republic of China
[3] Department of Electrical, Computer and System Engineering, Rensselaer Polytechnic Institute, Troy, NY 12180, USA

E-mail: yazici@ecse.rpi.edu

Received 15 October 2009, in final form 23 March 2010
Published 21 May 2010
Online at stacks.iop.org/IP/26/065006

Abstract

In this paper we consider passive airborne receivers that use backscattered signals from sources of opportunity transmitting single-frequency or ultra-narrowband waveforms. Because of its combined passive synthetic aperture and the single-frequency nature of the transmitted waveforms, we refer to the system under consideration as Doppler synthetic aperture hitchhiker (DSAH). We present a novel image formation method for DSAH. Our method first correlates the windowed signal obtained from one receiver with the windowed, filtered, scaled and translated version of the received signal from another receiver. This processing removes the transmitter-related variables from the phase of the Fourier integral operator that maps the radiance of the scene to the correlated signal. Next, we use microlocal analysis to reconstruct the scene radiance by the weighted backprojection of the correlated signal. The image reconstruction method is applicable to both cooperative and non-cooperative sources of opportunity using one or more airborne receivers. It has the desirable property of preserving the visible edges of the scene radiance. Additionally, it is an analytic reconstruction technique that can be made computationally efficient. We present numerical simulations to demonstrate the performance of the image reconstruction method and to verify the theoretical results.

(Some figures in this article are in colour only in the electronic version)

1. Introduction

In recent years, there has been a growing interest in passive radar applications using sources of opportunity [1–3]. This research effort is motivated by the growing availability of transmitters of opportunity, such as radio, television and cell phone stations, particularly in urban areas, as well as relatively low cost and rapid deployment of passive receivers.

While many passive radar applications are focused on the detection of airborne targets with ground-based receivers [1–5], recently, a number of methods for passive synthetic aperture radar have been developed [6, 7]. The methods presented in [1–5, 7] require either the knowledge of the transmitter locations and transmitted waveforms or receivers with high directivity that are within the transmitters' antenna beams. The direct line-of-sight to the transmitters is then used to estimate the transmitted waveforms and the transmitter location to perform matched filtering. In [6], we reported a novel passive synthetic aperture imaging method based on the spatio-temporal correlation of the received signal and the filtered backprojection technique. Unlike the methods in [1–5, 7], this method does not require receivers with high directivity or *a priori* knowledge about the transmitter locations and transmitted waveforms. The resolution analysis of the method shows that it is suitable for high-range-resolution waveforms, such as wideband pulses. However, most of the transmitters of opportunity, such as radio and TV stations, transmit single-frequency or ultra-narrowband waveforms. In this paper, we present a new passive synthetic aperture imaging method using sources of opportunity transmitting single-frequency or ultra-narrowband waveforms. These waveforms are also referred to as high-Doppler-resolution or continuous-wave (CW) waveforms. Thus, we refer to the resulting method as the *Doppler synthetic aperture hitchhiker* (DSAH) imaging method.

For each pair of receivers, our method first correlates the windowed signal obtained from one of the receivers with the windowed, filtered, scaled and translated version of the received signal from another receiver. The high-frequency analysis of the resulting forward model shows that the windowed, filtered, scaled and translated correlation of the received signals is the projections of the scene radiance onto the hitchhiker iso-Doppler curves that we introduced in [6]. We use microlocal techniques to develop a weighted backprojection reconstruction of the scene radiance. The analysis of the point spread function of the imaging operator shows that the reconstructed images preserve the location and orientation of the singularities at the intersection of the hitchhiker iso-Doppler and hitchhiker iso-Doppler-rate curves introduced in this paper. The final image of the scene radiance is formed by superposition of the images obtained for each pair of receivers at each time translation over a range of time translations. Note that if only a single receiver is available, the received signal is windowed, filtered, scaled and correlated with itself.

Our passive imaging method has the following advantages: (1) as compared to existing passive radar detection systems [2, 8–14], it does not require receivers with high directivity; (2) it can be used in the presence of both cooperative and non-cooperative sources of opportunity; (3) it can be used with stationary and/or mobile sources of opportunity; (4) it can be used with one or more airborne receivers; (5) it can be used under non-ideal imaging scenarios such as arbitrary flight trajectories and non-flat topography; (6) it has the desirable property of preserving the visible edges of the scene radiance in the reconstructed image. Additionally, it is an analytic image formation method that can be made computationally efficient.

The organization of our paper is as follows. In section 2.1, we develop the forward model for DSAH and analyze the leading-order contributions to the windowed, filtered, scaled and correlated measurements. In section 3, we develop a weighted backprojection-type image formation method for DSAH and analyze the underlying geometry and resolution of DSAH image formation. In section 4, we present numerical simulations to verify the theoretical results and demonstrate the performance of the DSAH image formation method. Finally, in section 5 we summarize our results and conclude our discussion. The paper includes two appendices including intermediate results needed for the image reconstruction method.

Table 1 lists notations used throughout the paper.

Table 1. Table of notations.

Symbol	Designation
$\mathbf{T}$	transmitter location
$\mathbf{R}$	receiver location
c_0	speed of light in free space
ω_0	frequency of single-frequency waveform
t	time variable
$f(t, \mathbf{R}, \mathbf{T})$	received signal at $\mathbf{R}$ due to a transmitter at $\mathbf{T}$
$\mathbf{z}_\psi = (z, \psi(z))$	earth's surface
$V(\mathbf{z})$	reflectivity function
$\rho(z)$	surface reflectivity
$\delta(z)$	Dirac delta function
$\widehat{\mathbf{z}}$	unit vector in the direction of $\mathbf{z} \in \mathbb{R}^3$
$\gamma_i(t)$	flight trajectory of the ith receiver
$s_{ij}(t) = f(t, \gamma_i(t), \mathbf{T})$	signal collected along the receiver trajectory $\gamma_i(t)$ due to a transmitter located at $\mathbf{T}$
τ, τ'	variables for temporal translation
μ	temporal scaling factor
$\phi(t)$	temporal windowing function
$B_{ij}(z_0, t, \tau', \tau, \mu)$	reconstruction filter
$c_{ij}(\tau', \tau, \mu)$	windowed, filtered, scaled and translated correlations of the received signals from the ith and jth receiver trajectories
$R_\rho(z)$	scene radiance
$R_T(\omega_0, z, z', \mathbf{T})$	transmitter irradiance
$A_{R_{ij}}(\omega_0, z, z', t, \tau', \tau, \mu)$	product of the receiver antenna beam patterns
$G_{ij}(\mathbf{z}, \mathbf{z}', t, \tau', \tau, \mu)$	product of the geometric spreading factors due to transmitter $\mathbf{T}$ and receivers i and j
$\mathcal{F}_{ij}$	forward modeling operator
$\varphi_{ij}(t, z, \tau', \tau, \mu)$	phase of the operator $\mathcal{F}_{ij}$
$\dfrac{A_{ij}(z, t, \tau', \tau, \mu)}{B_{ij}(z_0, t, \tau', \tau, \mu)}$	amplitude of the operator $\mathcal{F}_{ij}$
$S_{ij}(\tau', \tau, \mathbf{z})$	Doppler hitchhiker scale factor
$F_{ij}(\tau', \tau, \mu)$	hitchhiker iso-Doppler contour
$\dot{F}_j(\tau, C)$	hitchhiker iso-Doppler rate contour
v_i	radial velocity of the ith receiver with respect to $\mathbf{z} \in \mathbb{R}^3$
$\widetilde{R}_\rho(z)$	image of the scene radiance
$\mathcal{K}$	weighted backprojection operator
$Q_{ij}(z, \tau', \tau)$	reconstruction weight
$L(z, z')$	point spread function
$\Omega_{ij,\tau',z}$	partial data collection manifold at (τ', z) due to the ith and jth receivers
Ω_z	data collection manifold at $\mathbf{z} \in \mathbb{R}^3$
L_ϕ	length of the support of $\phi(t)$

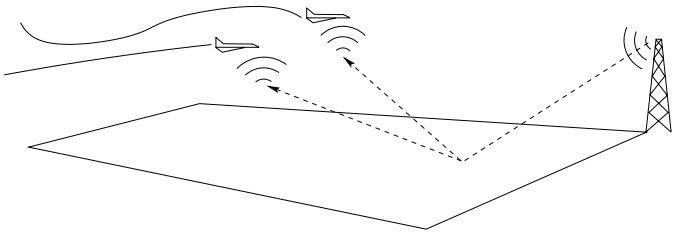

Figure 1. An illustration of the DSAH imaging geometry.

2. DSAH measurement model

2.1. Model for the received signal

We use the following notational conventions throughout the paper. The bold Roman, bold italic and Roman lowercase letters are used to denote variables in $\mathbb{R}^3$, $\mathbb{R}^2$ and $\mathbb{R}$, respectively, i.e. $\mathbf{z} = (\boldsymbol{z}, z) \in \mathbb{R}^3$, with $\boldsymbol{z} \in \mathbb{R}^2$ and $z \in \mathbb{R}$. The calligraphic letters ($\mathcal{F}$, $\mathcal{K}$ etc) are used to denote operators.

Given a pair of transmitter and receiver antennas located at $\mathbf{T}$ and $\mathbf{R}$ respectively, we model the received signal by [15]

$$f(t, \mathbf{R}, \mathbf{T}) \approx \int \frac{\mathrm{e}^{-\mathrm{i}\omega(t-(|\mathbf{R}-\mathbf{z}|+|\mathbf{z}-\mathbf{T}|)/c_0)}}{(4\pi)^2|\mathbf{R}-\mathbf{z}||\mathbf{z}-\mathbf{T}|}\omega^2 \times J_{\mathrm{tr}}(\omega, \widehat{\mathbf{z}-\mathbf{T}}, \mathbf{T}) J_{\mathrm{rc}}(\omega, \widehat{\mathbf{z}-\mathbf{R}}, \mathbf{R}) V(\mathbf{z})\, \mathrm{d}\omega\, \mathrm{d}\mathbf{z}, \tag{1}$$

where t denotes time, c_0 denotes the speed of light in free space, $V(\mathbf{z})$ is the reflectivity function and J_{tr} and J_{rc} are the transmitter and receiver antenna beam patterns, respectively.

We make the assumption that the earth's surface is located at a position given by $\mathbf{z} = (\boldsymbol{z}, \psi(\boldsymbol{z})) \in \mathbb{R}^3$, where $\boldsymbol{z} \in \mathbb{R}^2$ and $\psi : \mathbb{R}^2 \to \mathbb{R}$ is a known function for the ground topography. Furthermore, we assume that the scattering takes place in a thin region near the surface. Thus, the reflectivity function is in the form

$$V(\mathbf{z}) = \rho(\boldsymbol{z})\delta(z - \psi(\boldsymbol{z})). \tag{2}$$

Under these assumptions, for a single-frequency or ultra-narrowband waveform at frequency ω_0, the received signal model in (1) becomes

$$f(t, \mathbf{R}, \mathbf{T}) \approx \int \frac{\mathrm{e}^{-\mathrm{i}\omega_0(t-(|\mathbf{R}-\mathbf{z}|+|\mathbf{z}-\mathbf{T}|)/c_0)}}{(4\pi)^2|\mathbf{R}-\mathbf{z}||\mathbf{z}-\mathbf{T}|}\omega_0^2 \times J_{\mathrm{tr}}(\omega_0, \widehat{\mathbf{z}-\mathbf{T}}, \mathbf{T}) J_{\mathrm{rc}}(\omega_0, \widehat{\mathbf{z}-\mathbf{R}}, \mathbf{R}) \rho(\boldsymbol{z})\, \mathrm{d}\boldsymbol{z}, \tag{3}$$

where $\widehat{\mathbf{z}} = \mathbf{z}/|\mathbf{z}|$ denotes the unit vector in the direction of $\mathbf{z} \in \mathbb{R}^3$. For the rest of the paper, unless otherwise stated, we use $\mathbf{z} = \mathbf{z}(\boldsymbol{z}) = (\boldsymbol{z}, \psi(\boldsymbol{z}))$.

Our imaging method is applicable to both mobile and stationary sources of opportunity. However, for the rest of our discussion, we assume that there is a single, stationary transmitter of opportunity illuminating the scene. This allows us to simplify the analysis and distill the important aspects that can readily be generalized using the ideas similar to the ones presented in our work [6].

Let $\mathbf{T} \in \mathbb{R}^3$ denote the location of the transmitter of opportunity and let there be N airborne receivers, each traversing a smooth trajectory $\boldsymbol{\gamma}_i(t)$, $i = 1, \ldots, N$, as shown in figure 1.

We define

$$s_i(t) = f(t, \gamma_i(t), \mathbf{T}) \tag{4}$$

as the received signal by the ith receiver, $i = 1, \ldots, N$.

Note that for multiple transmitters and multiple transmit frequencies, the signal received by the ith receiver becomes

$$s_i(t) = \int f(t, \gamma_i(t), \mathbf{T})\, \mathrm{d}\mathbf{T}\, \mathrm{d}\omega_0. \tag{5}$$

Since each transmitted frequency can be isolated with appropriate bandbass filtering, without loss of generality, we perform our analysis with respect to a fixed frequency ω_0.

2.2. *Windowed, filtered, scaled and translated correlation of received signals*

For a given point of interest $\boldsymbol{z}_0$ on the ground topography and a fixed $\tau' \in \mathbb{R}$, we define the windowed, filtered scaled, and translated correlation of the received signals s_i and s_j by

$$c_{ij}^{\boldsymbol{z}_0}(\tau', \tau, \mu) = \int \frac{s_i(t + \tau') s_j^*(\mu t + \tau)}{B_{ij}(\boldsymbol{z}_0, t, \tau', \tau, \mu)}\, \phi(t)|t|\, \mathrm{d}t, \tag{6}$$

for some $\tau, \tau' \in \mathbb{R}$ and $\mu \in \mathbb{R}^+$, $i, j = 1, \ldots, N$, where $\phi(t)$ is a smooth compactly supported temporal windowing function centered at $t = 0$, B_{ij} is a filter to be determined later and * denotes the complex conjugation. To simplify our notation, we drop the superscripts $\boldsymbol{z}_0$ from $c_{ij}^{\boldsymbol{z}_0}(\tau', \tau, \mu)$ for the rest of our paper.

Note that for a single receiver, we only have $c_{ij} = c_{11}$.

In the following subsections, we develop a mapping that relates the expected value of the correlated measurements c_{ij} to the scene to be imaged for both cooperative and non-cooperative sources of opportunity. We assume that for non-cooperative sources of opportunity, the location of the transmitter, $\mathbf{T}$, and transmitter antenna beam pattern J_{tr} are unknown. For cooperative sources of opportunity, we assume that these quantities are known. For both cases, we assume that the frequency of the transmitted waveform ω_0 is known.

2.2.1. Non-cooperative sources of opportunity. For non-cooperative sources of opportunity, we use a stochastic model for the transmitter antenna beam pattern, J_{tr}, and the scene reflectivity, ρ.

Let C_ρ and $C_{J_{\mathrm{tr}}}$ denote the correlation function of ρ and J_{tr}, respectively,

$$C_\rho(\boldsymbol{z}, \boldsymbol{z}') = E[\rho(\boldsymbol{z})\rho^*(\boldsymbol{z}')] \tag{7}$$

$$C_{J_{\mathrm{tr}}}(\omega_0, \boldsymbol{z}, \boldsymbol{z}', \mathbf{T}) = E[J_{\mathrm{tr}}(\omega_0, \widehat{\mathbf{z} - \mathbf{T}}, \mathbf{T}) J_{\mathrm{tr}}^*(\omega_0, \widehat{\mathbf{z}' - \mathbf{T}}, \mathbf{T})]. \tag{8}$$

We assume that the scene reflectivity ρ and the transmit antenna beam pattern J_{tr} are statistically independent. Next, we make the incoherent-field approximation [16] by assuming that ρ and J_{tr} satisfy the following equalities:

$$C_\rho(\boldsymbol{z}, \boldsymbol{z}') = R_\rho(\boldsymbol{z})\delta(\boldsymbol{z} - \boldsymbol{z}'). \tag{9}$$

$$C_{J_{\mathrm{tr}}}(\omega_0, \boldsymbol{z}, \boldsymbol{z}', \mathbf{T}) = R_T(\omega_0, \boldsymbol{z}, \boldsymbol{z}', \mathbf{T})\delta(\boldsymbol{z} - \boldsymbol{z}'). \tag{10}$$

Note that R_ρ is the average power of the electromagnetic radiation emitted by the scene at location $\boldsymbol{z}$, and R_T is the average power of the electromagnetic radiation emitted by the

transmitter at location $\mathbf{T}$ that is incident on the target surface at z. In this regard, R_ρ is referred to as the *scene radiance* and R_T is referred to as the transmitter irradiance [16].

Substituting s_i and s_j into c_{ij}, under the assumption that ρ, J_{tr} and $|\mathbf{T}-\mathbf{z}|$ are statistically independent, and using (9) and (10), we express the expectation of c_{ij} as

$$\begin{aligned} E[c_{ij}(\tau',\tau,\mu)] = \frac{\omega_0^4}{(4\pi)^4}\int \mathrm{e}^{-\mathrm{i}\omega_0(t+\tau'-(|\gamma_i(t+\tau')-\mathbf{z}|+|\mathbf{T}-\mathbf{z}|)/c_0)}\,\mathrm{e}^{\mathrm{i}\omega_0(\mu t+\tau-(|\gamma_j(\mu t+\tau)-\mathbf{z}'|+|\mathbf{T}-\mathbf{z}'|)/c_0)} \\ \times \frac{R_T(\omega_0,z,z',\mathbf{T})A_{R_{ij}}(\omega_0,z,z',t,\tau',\tau,\mu)}{G_{ij}(\mathbf{z},\mathbf{z}',t,\tau',\tau,\mu)B_{ij}(z_0,t,\tau',\tau,\mu)} \\ \times R_\rho(z)\delta(z-z')\,\mathrm{d}z\,\mathrm{d}z'\,\phi(t)|t|\,\mathrm{d}t, \end{aligned} \tag{11}$$

where $A_{R_{ij}}$ is the product of the receiver antenna beam patterns,

$$\begin{aligned} A_{R_{ij}}(\omega_0,z,z',t,\tau',\tau,\mu) = J_{\mathrm{rc}}(\omega_0,\mathbf{z}-\widehat{\gamma_i(t+\tau')},\gamma_i(t+\tau')) \\ \times J_{\mathrm{rc}}^*(\omega_0,\mathbf{z}'-\widehat{\gamma_j(\mu t+\tau)},\gamma_j(\mu t+\tau)), \end{aligned} \tag{12}$$

and G_{ij} is the product of the geometric spreading factors:

$$G_{ij}(\mathbf{z},\mathbf{z}',t,\tau',\tau,\mu) = |\mathbf{T}-\mathbf{z}||\mathbf{T}-\mathbf{z}'||\gamma_i(t+\tau')-\mathbf{z}||\gamma_j(\mu t+\tau)-\mathbf{z}'|. \tag{13}$$

Note that for non-cooperative sources of opportunity, $\mathbf{T}$, and thus $|\mathbf{T}-\mathbf{z}||\mathbf{T}-\mathbf{z}'|$, are unknown.

Now using the Taylor series expansion at $t=0$,

$$\gamma_i(t+\tau') = \gamma_i(\tau')+\dot\gamma_i(\tau')t+\cdots \tag{14}$$

$$\gamma_j(\mu t+\tau) = \gamma_j(\tau)+\dot\gamma_j(\tau)\mu t+\cdots, \tag{15}$$

we approximate

$$\begin{aligned} |\gamma_i(t+\tau')-\mathbf{z}| &\approx |\gamma_i(\tau')-\mathbf{z}+\dot\gamma_i(\tau')t| \\ &\approx |\gamma_i(\tau')-\mathbf{z}|+(\widehat{\gamma_i(\tau')-\mathbf{z}})\cdot\dot\gamma_i(\tau')t \end{aligned} \tag{16}$$

and

$$\begin{aligned} |\gamma_j(\mu t+\tau)-\mathbf{z}'| &\approx |\gamma_j(\tau)-\mathbf{z}'+\dot\gamma_j(\tau)\mu t| \\ &\approx |\gamma_j(\tau)-\mathbf{z}'|+(\widehat{\gamma_j(\tau)-\mathbf{z}'})\cdot\dot\gamma_j(\tau)\mu t. \end{aligned} \tag{17}$$

Substituting approximations (16) and (17) into (11), and performing the z' integration, we have

$$\begin{aligned} E[c_{ij}(\tau',\tau,\mu)] &\approx \mathcal{F}_{ij}[R_\rho](\tau,\mu) \\ &= \int \mathrm{e}^{-\mathrm{i}\varphi_{ij}(t,z,\tau',\tau,\mu)}\,\frac{A_{ij}(z,t,\tau',\tau,\mu)}{B_{ij}(z_0,t,\tau',\tau,\mu)}\,R_\rho(z)\,\mathrm{d}z\,|t|\,\mathrm{d}t, \end{aligned} \tag{18}$$

where

$$\varphi_{ij}(t,z,\tau',\tau,\mu) = \omega_0 t[1-(\widehat{\gamma_j(\tau)-\mathbf{z}})\cdot\dot\gamma_j(\tau)/c_0][S_{ij}(\tau',\tau,\mathbf{z})-\mu], \tag{19}$$

with

$$S_{ij}(\tau',\tau,\mathbf{z}) = \frac{1-(\widehat{\gamma_i(\tau')-\mathbf{z}})\cdot\dot\gamma_i(\tau')/c_0}{1-(\widehat{\gamma_j(\tau)-\mathbf{z}})\cdot\dot\gamma_j(\tau)/c_0} \tag{20}$$

and

$$\begin{aligned} A_{ij}(z,t,\tau',\tau,\mu) = \frac{\tilde R_T(\omega_0,z)A_{R_{ij}}(\omega_0,z,z,t,\tau',\tau,\mu)}{G_{ij}(\mathbf{z},\mathbf{z},t,\tau',\tau,\mu)} \\ \times \frac{\omega_0^4\phi(t)}{(4\pi)^4}\,\mathrm{e}^{-\mathrm{i}\omega_0(\tau'-\tau-(|\gamma_i(\tau')-\mathbf{z}|-|\gamma_j(\tau)-\mathbf{z}|)/c_0)}, \end{aligned} \tag{21}$$

with $\tilde{R}_T(\omega_0, \boldsymbol{z}) = R_T(\omega_0, \boldsymbol{z}, \boldsymbol{z}, \mathbf{T})$. We refer to $S_{ij}(\tau', \tau, \mathbf{z})$ as the *Doppler hitchhiker scale factor*, and φ_{ij} and A_{ij}/B_{ij} as the phase and amplitude terms of the linear operator $\mathcal{F}_{ij}$, respectively.

Note that the filtered, scaled and translated correlation of the received signal removes all transmitter-related terms from the phase of the operator $\mathcal{F}_{ij}$.

2.2.2. Cooperative sources of opportunity. If the sources of opportunity are cooperative, we use a stochastic model for the unknown scene reflectivity ρ, but assume that the transmitter locations and antenna beam patterns are known. Thus, we treat J_{tr} deterministically.

In this case, the expected value of c_{ij} is given by

$$\begin{aligned} E[c_{ij}(\tau', \tau, \mu)] = \frac{\omega_0^4}{(4\pi)^4} \int & \mathrm{e}^{-\mathrm{i}\omega_0(t+\tau'-(|\gamma_i(t+\tau')-\mathbf{z}|+|\mathbf{T}-\mathbf{z}|)/c_0)} \, \mathrm{e}^{\mathrm{i}\omega_0(\mu t+\tau-(|\gamma_j(\mu t+\tau)-\mathbf{z}'|+|\mathbf{T}-\mathbf{z}'|)/c_0)} \\ & \times \frac{B_T(\omega_0, \boldsymbol{z}, \boldsymbol{z}', \mathbf{T}) A_{R_{ij}}(\omega_0, \boldsymbol{z}, \boldsymbol{z}', t, \tau', \tau, \mu)}{G_{ij}(\mathbf{z}, \mathbf{z}', t, \tau', \tau, \mu) B_{ij}(\boldsymbol{z}_0, t, \tau', \tau, \mu)} \\ & \times C_\rho(\boldsymbol{z}, \boldsymbol{z}') \, \mathrm{d}\boldsymbol{z} \, \mathrm{d}\boldsymbol{z}' \, \phi(t)|t| \, \mathrm{d}t, \end{aligned} \tag{22}$$

where C_ρ is the correlation function of ρ given in (7), $A_{R_{ij}}$ and G_{ij} are as defined in (12) and (13), respectively, and

$$B_T(\omega_0, \boldsymbol{z}, \boldsymbol{z}', \mathbf{T}) = J_{\mathrm{tr}}(\omega_0, \widehat{\mathbf{z} - \mathbf{T}}, \mathbf{T}) J_{\mathrm{tr}}^*(\omega_0, \widehat{\mathbf{z}' - \mathbf{T}}, \mathbf{T}). \tag{23}$$

Next, we make the incoherent-field approximation given in (9) and substitute the Taylor series expansion in (16) and (17) into (22). Thus, (22) simplifies to

$$\begin{aligned} E[c_{ij}(\tau', \tau, \mu)] &\approx \mathcal{F}_{ij}[R_\rho](\tau, \mu) \\ &= \int \mathrm{e}^{-\mathrm{i}\varphi_{ij}(t, \boldsymbol{z}, \tau', \tau, \mu)} \frac{A_{ij}(\boldsymbol{z}, t, \tau', \tau, \mu)}{B_{ij}(\boldsymbol{z}_0, t, \tau', \tau, \mu)} R_\rho(\boldsymbol{z})|t| \, \mathrm{d}\boldsymbol{z} \, \mathrm{d}t, \end{aligned} \tag{24}$$

where

$$\varphi_{ij}(t, \boldsymbol{z}, \tau', \tau, \mu) = \omega_0 t[1 - (\widehat{\gamma_j(\tau) - \mathbf{z}}) \cdot \dot{\gamma}_j(\tau)/c_0][S_{ij}(\tau', \tau, \mathbf{z}) - \mu], \tag{25}$$

$$\begin{aligned} A_{ij}(\boldsymbol{z}, t, \tau', \tau, \mu) = & \frac{\tilde{R}_T(\omega_0, \boldsymbol{z}) A_{R_{ij}}(\omega_0, \boldsymbol{z}, \boldsymbol{z}, t, \tau', \tau, \mu)}{G_{ij}(\mathbf{z}, \mathbf{z}, t, \tau', \tau, \mu)} \\ & \times \frac{\omega_0^4 \, \phi(t)}{(4\pi)^4} \mathrm{e}^{-\mathrm{i}\omega_0(\tau'-\tau-(|\gamma_i(\tau')-\mathbf{z}|-|\gamma_j(\tau)-\mathbf{z}|)/c_0)}, \end{aligned} \tag{26}$$

with $\tilde{R}_T(\omega_0, \boldsymbol{z}) = B_T(\omega_0, \boldsymbol{z}, \boldsymbol{z}, \mathbf{T})$. S_{ij} in (25) is the Doppler hitchhiker scale factor defined in (20).

We refer to $\mathcal{F}_{ij}$ defined in (18)–(21) and (24)–(26) as the DSAH forward modeling operator. Note that (24) and (18) are exactly the same, with the exception that $\tilde{R}_T$ in (26) is given as a function of the deterministic transmit antenna beam pattern for the cooperative sources of opportunity, whereas $\tilde{R}_T$ in (21) is given as a function of the correlation function of the transmit antenna beam pattern for the non-cooperative sources of opportunity. Thus, the inversion formula for (24) and (18) will be the same.

2.3. Leading-order contribution to the windowed, filtered, scaled and translated correlations

We assume that for some m_A, A_{ij}/B_{ij} satisfies the inequality

$$\sup_{(t,\mu,\tau,\boldsymbol{z}) \in \mathcal{U}} \left| \partial_t^{\alpha_t} \partial_\mu^{\alpha_\mu} \partial_\tau^\beta \partial_{z_1}^{\epsilon_1} \partial_{z_2}^{\epsilon_2} \frac{A_{ij}(\boldsymbol{z}, t, \tau', \tau, \mu)}{B_{ij}(\boldsymbol{z}_0, t, \tau', \tau, \mu)} |t| \right| \leqslant C_A (1 + t^2)^{(m_A - |\alpha_t|)/2}, \tag{27}$$

where $\mathcal{U}$ is any compact subset of $\mathbb{R}^+ \times \mathbb{R}^+ \times \mathbb{R} \times \mathbb{R}^2$, and the constant C_A depends on $\mathcal{U}, \alpha_{t,\mu}, \beta, \epsilon_{1,2}$. This assumption is needed to make various stationary phase calculations hold. In practice, with appropriate choice of B_{ij}, (27) is satisfied for transmitters and receivers sufficiently far away from the illuminated region.

Under the assumption (27), both (18) and (24) define $\mathcal{F}$ as a *Fourier integral operator* whose leading-order contributions come from those points lying in the intersection of the illuminated surface $(z, \psi(z))$ and points that have the same Doppler hitchhiker scale factor, i.e. $\{\mathbf{z} \in \mathbb{R}^3 : S_{ij}(\tau', \tau, \mathbf{z}) = \mu\}$. We denote the curves formed by this intersection by

$$F_{ij}(\tau', \tau, \mu) = \{z : S_{ij}(\tau', \tau, \mathbf{z} = (z, \psi(z))) = \mu\}. \tag{28}$$

When the speed of the receivers is much slower than the speed of light c_0, S_{ij} can be approximated as follows:

$$\begin{aligned} S_{ij}(\tau', \tau, \mathbf{z}) &= 1 + \frac{(\widehat{\gamma_j(\tau) - \mathbf{z}}) \cdot \dot{\gamma}_j(\tau)/c_0 - (\widehat{\gamma_i(\tau') - \mathbf{z}}) \cdot \dot{\gamma}_i(\tau')/c_0}{1 - (\widehat{\gamma_j(\tau) - \mathbf{z}}) \cdot \dot{\gamma}_j(\tau)/c_0} \\ &\approx 1 + [(\widehat{\gamma_j(\tau) - \mathbf{z}}) \cdot \dot{\gamma}_j(\tau) - (\widehat{\gamma_i(\tau') - \mathbf{z}}) \cdot \dot{\gamma}_i(\tau')]/c_0. \end{aligned} \tag{29}$$

Substituting (29) into

$$S_{ij}(\tau', \tau, \mathbf{z}) = \mu, \tag{30}$$

multiplying both sides of (30) by ω_0, and rearranging the terms, we have

$$\frac{\omega_0}{c_0}[(\widehat{\gamma_i(\tau') - \mathbf{z}}) \cdot \dot{\gamma}_i(\tau') - (\widehat{\gamma_j(\tau) - \mathbf{z}}) \cdot \dot{\gamma}_j(\tau)] = (1 - \mu)\omega_0, \tag{31}$$

where the left-hand side of (31) is the hitchhiker Doppler defined in [6] for a fixed frequency. In this regard, we refer to $F_{ij}(\tau', \tau, \mu)$ as the DSAH iso-Doppler contour. Figure 2 shows the DSAH iso-Doppler contours for two receivers traversing a circular trajectory over a flat topography.

Note that (30) can be expressed as

$$(\widehat{\gamma_i(\tau') - \mathbf{z}}) \cdot \dot{\gamma}_i(\tau') - \mu(\widehat{\gamma_j(\tau) - \mathbf{z}}) \cdot \dot{\gamma}_j(\tau) = (1 - \mu)c_0. \tag{32}$$

The first term above is the radial velocity of the ith receiver in the direction of $\widehat{\gamma_i(\tau') - \mathbf{z}}$, and the second term is the radial velocity of the jth receiver in the direction of $\widehat{\gamma_j(\tau) - \mathbf{z}}$ scaled by μ. Let v_i be the radial velocity of the ith receiver with respect to $\mathbf{z}$. Then, the curves $F_{ij}(\tau', \tau, \mu)$, where $\mathcal{F}_{ij}$ projects the scene radiance R_ρ, are formed by the intersection of the constant-Doppler cones

$$(\widehat{\gamma_i(\tau') - \mathbf{z}}) \cdot \dot{\gamma}_i(\tau') = v_i \tag{33}$$

and

$$(\widehat{\gamma_j(\tau) - \mathbf{z}}) \cdot \dot{\gamma}_j(\tau) = [v_i - (1 - \mu)c_0]/\mu, \tag{34}$$

and the earth's surface.

For flat topography, (33) and (34) define hyperbolas, which we denote by $H_{i,\tau',\tau}(v_i)$ and $H_{j,\tau',\tau,\mu}(v_i)$, respectively. Thus, $F_{ij}(\tau', \tau, \mu)$ can be parameterized by v_i and defined by the points in the intersection of $H_{i,\tau',\tau}(v_i)$ and $H_{j,\tau',\tau,\mu}(v_i)$ as follows:

$$F_{ij}(\tau', \tau, \mu) = \left\{ z \in \mathbb{R}^2 \,\middle|\, z \in \bigcup_{v_i \in \mathbb{R}} \left[H_{i,\tau',\tau}(v_i) \bigcap H_{j,\tau',\tau,\mu}(v_i) \right] \right\}. \tag{35}$$

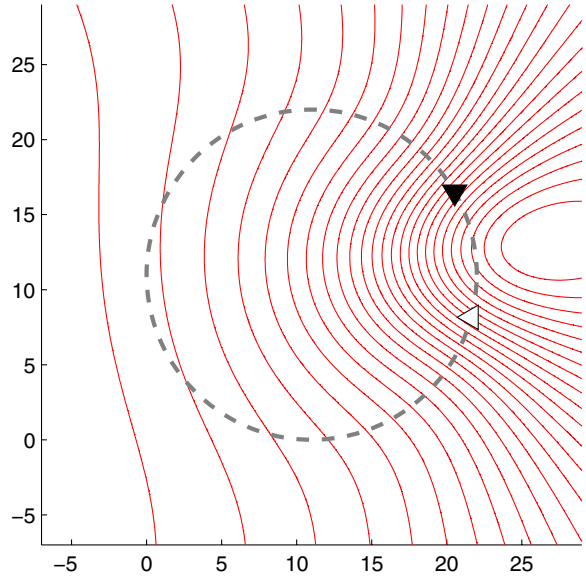

Figure 2. Iso-Doppler contours $F_{ij}(\tau', \tau, \mu)$ for the Doppler hitchhiker scale factor $S_{12}(\pi/6, -\pi/12, \mathbf{z})$. Two receivers are traversing a circular flight trajectory (dashed line) at the speed of 261 m s^{-1} over a flat topography. $\gamma_1(s) = \gamma_C(s)$ and $\gamma_2(s) = \gamma_C(s - \pi/4)$, respectively, where white and black triangles denote the positions of the two receivers at $s = \pi/6$, respectively. (See (20) and (73) for explicit formulas of $S_{12}(\pi/6, -\pi/12, \mathbf{z})$ and $\gamma_C(s)$, respectively.)

3. Image formation

Our objective is to form an image of the scene radiance $R_\rho(\mathbf{z})$ using $E[c_{ij}(\tau', \tau, \mu)]$, $i, j = 1, \ldots, N$, for a range of τ', τ and μ values based on the forward model (18) or (24).

Since $\mathcal{F}_{ij}$ is a Fourier integral operator, we form an image of the scene radiance by a suitable weighted backprojection of $E[c_{ij}(\tau', \tau, \mu)]$ onto $F_{ij}(\tau', \tau, \mu)$, $i, j = 1, \ldots, N$ [17].

3.1. Weighted backprojection operator

We form an image of the scene radiance by the superposition of the weighted and backprojected data, $E[c_{ij}(\tau, \mu)]$, as follows:

$$\tilde{R}_\rho(\mathbf{z}) = \sum_{ij} \int \mathcal{K}_{ij}[E[c_{ij}]](\mathbf{z}, \tau')\, \mathrm{d}\tau'$$

where

$$\mathcal{K}_{ij}[E[c_{ij}]](\mathbf{z}, \tau') = \int \mathrm{e}^{\mathrm{i}\varphi_{ij}(t, \mathbf{z}, \tau', \tau, \mu)} Q_{ij}(\mathbf{z}, \tau', \tau, \mu) E[c_{ij}(\tau', \tau, \mu)]\, \mathrm{d}t\, \mathrm{d}\tau\, \mathrm{d}\mu. \tag{36}$$

We refer to $\mathcal{K}_{ij}$ as the weighted backprojection operator with respect to the ith and jth receivers, with weight Q_{ij} to be determined below.

We will show that the weighted backprojection operator reconstructs the visible edges of the scene at the correct location and correct orientation irrespective of the choice of the weights, Q_{ij}.

3.2. The point spread function

We rewrite $\tilde{R}_\rho$ as

$$\tilde{R}_\rho(z) = \sum_{ij} \mathcal{K}_{ij}\mathcal{F}_{ij}[R_\rho](z) = \int L(z, z')R_\rho(z')\,\mathrm{d}z', \tag{37}$$

where $L(z, z')$ is the *point spread function* (PSF) of the imaging operator given by

$$L(z, z') = \sum_{ij} \int L_{ij}(z, z', \tau')\,\mathrm{d}\tau' \tag{38}$$

and

$$L_{ij}(z, z', \tau') = \int \mathrm{e}^{\mathrm{i}[\varphi_{ij}(t,z,\tau',\tau,\mu)-\varphi_{ij}(t',z',\tau',\tau,\mu)]}\, Q_{ij}(z, \tau', \tau, \mu) \times \frac{A_{ij}(z', t, \tau', \tau, \mu)}{B_{ij}(z, t, \tau', \tau, \mu)}\,|t|\,\mathrm{d}t'\,\mathrm{d}t\,\mathrm{d}\tau\,\mathrm{d}\mu. \tag{39}$$

Note that $L_{ij}(z, z', \tau')$ can be viewed as the point spread function of the partial imaging operator $\mathcal{K}_{ij}$.

We next define

$$\Phi_K := \varphi_{ij}(t, z, \tau', \tau, \mu) - \varphi_{ij}(t', z', \tau', \tau, \mu) \tag{40}$$

as the phase of $\mathcal{K}_{ij}\mathcal{F}_{ij}$ and use the stationary phase theorem [18–21] to approximate the t' and μ integrations. We compute

$$\partial_{t'}\Phi_K = -\omega_0[1 - (\widehat{\gamma_j(\tau) - \mathbf{z}'}) \cdot \dot{\gamma}_j(\tau)/c_0][S_{ij}(\tau', \tau, z') - \mu] \tag{41}$$

and

$$\partial_\mu\Phi_K = -\omega_0 t\,(1 - (\widehat{\gamma_j(\tau) - \mathbf{z}}) \cdot \dot{\gamma}_j(\tau)/c_0) + \omega_0 t'(1 - (\widehat{\gamma_j(\tau) - \mathbf{z}'}) \cdot \dot{\gamma}_j(\tau)/c_0). \tag{42}$$

The stationary points of the phase satisfy $\partial_{t',\mu}\Phi_K = 0$, implying that

$$\mu = \frac{1 - (\widehat{\gamma_i(\tau') - \mathbf{z}'}) \cdot \dot{\gamma}_i(\tau')/c_0}{1 - (\widehat{\gamma_j(\tau) - \mathbf{z}'}) \cdot \dot{\gamma}_j(\tau)/c_0} = S_{ij}(\tau', \tau, \mathbf{z}') \tag{43}$$

and

$$t' = t\,\frac{1 - (\widehat{\gamma_j(\tau) - \mathbf{z}}) \cdot \dot{\gamma}_j(\tau)/c_0}{1 - (\widehat{\gamma_j(\tau) - \mathbf{z}'}) \cdot \dot{\gamma}_j(\tau)/c_0}. \tag{44}$$

Substituting (43) and (44) back into (39), we obtain

$$L_{ij}(z, z', \tau') \approx \int \mathrm{e}^{-\mathrm{i}\,\omega_0 t[1-(\widehat{\gamma_j(\tau)-\mathbf{z}})\cdot\dot{\gamma}_j(\tau)/c_0][S_{ij}(\tau',\tau,z')-S_{ij}(\tau',\tau,z)]} \times Q_{ij}(z, \tau', \tau, S_{ij}(\tau', \tau, z'))\frac{A_{ij}(z', t, \tau', \tau, S_{ij}(\tau', \tau, z'))}{B_{ij}(z, t, \tau', \tau, S_{ij}(\tau', \tau, z'))}|t|\,\mathrm{d}t\,\mathrm{d}\tau.$$

To simplify our notation, for the rest of our paper, we write

$$Q_{ij}(z, \tau', \tau) = Q_{ij}(z, \tau', \tau, S_{ij}(\tau', \tau, z)) \tag{46}$$

$$\begin{aligned} A_{ij}(z, t, \tau', \tau) &= A_{ij}(z, t, \tau', \tau, S_{ij}(\tau', \tau, z)) \\ B_{ij}(z, t, \tau', \tau) &= B_{ij}(z, t, \tau', \tau, S_{ij}(\tau', \tau, z)). \end{aligned} \tag{47}$$

Applying the method of the stationary phase to the t and τ integrals, we see that the main contribution to $L_{ij}(z, z', \tau')$ comes from those critical points of its phase that satisfy the conditions

$$\begin{aligned}\partial_t(\omega_0 t[1 - (\widehat{\gamma_j(\tau) - \mathbf{z}}) \cdot \dot{\gamma}_j(\tau)/c_0][S_{ij}(\tau', \tau, z') - S_{ij}(\tau', \tau, z)]) = 0 \\ \Rightarrow S_{ij}(\tau', \tau, z') = S_{ij}(\tau', \tau, z),\end{aligned} \tag{48}$$

and

$$\begin{aligned}\partial_\tau(\omega_0 t[1 - (\widehat{\gamma_j(\tau) - \mathbf{z}}) \cdot \dot{\gamma}_j(\tau)/c_0][S_{ij}(\tau', \tau, z') - S_{ij}(\tau', \tau, z)]) = 0 \\ \Rightarrow \frac{a_j^{\sum}(\tau, \mathbf{z})}{1 - (\widehat{\gamma_j(\tau) - \mathbf{z}}) \cdot \dot{\gamma}_j(\tau)/c_0} = \frac{a_j^{\sum}(\tau, \mathbf{z}')}{1 - (\widehat{\gamma_j(\tau) - \mathbf{z}'}) \cdot \dot{\gamma}_j(\tau)/c_0}\end{aligned} \tag{49}$$

where

$$a_j^{\sum}(\tau, \mathbf{z}) = \frac{1}{|\gamma_j(\tau) - \mathbf{z}|}|\dot{\gamma}_{j,\perp}(\tau, \mathbf{z})|^2 + (\widehat{\gamma_j(\tau) - \mathbf{z}}) \cdot \ddot{\gamma}_j(\tau) \tag{50}$$

and

$$\dot{\gamma}_{j,\perp}(\tau, \mathbf{z}) = \dot{\gamma}_j(\tau) - (\widehat{\gamma_j(\tau) - \mathbf{z}})((\widehat{\gamma_j(\tau) - \mathbf{z}}) \cdot \dot{\gamma}_j(\tau)). \tag{51}$$

Note that $\dot{\gamma}_{j,\perp}(\tau, \mathbf{z})$ is the projection of the receiver velocity $\dot{\gamma}_j(\tau)$ onto the plane whose normal direction is along $\widehat{\gamma_j(\tau) - \mathbf{z}}$ and $a_j^{\sum}(\tau, \mathbf{z})$ is the total relative radial acceleration of the jth receiver in the direction of $\widehat{\gamma_j(\tau) - \mathbf{z}}$. For the derivation of (49), see appendix A.

We define

$$f_j(\tau, \mathbf{z}) := \frac{a_j^{\sum}(\tau, \mathbf{z})}{1 - (\widehat{\gamma_j(\tau) - \mathbf{z}}) \cdot \dot{\gamma}_j(\tau)/c_0}. \tag{52}$$

We refer to $f_j(\tau, \mathbf{z})$ as the DSAH Doppler rate of the jth receiver. We refer to the locus of points formed by the intersection of the surface topography and $\{\mathbf{z} \in \mathbb{R}^3 : f_j(\tau, \mathbf{z}) = C\}$, for some constant C, as the DSAH iso-Doppler-rate contour, and denote it by

$$\dot{F}_j(\tau, C) = \{z : f_j(\tau, z) = C\}. \tag{53}$$

Figure 3 shows the DSAH iso-Doppler-rate contours with fixed τ for a circular flight trajectory and flat topography.

The critical points z of the phase of $L_{ij}(z, z', \tau')$ are those points lying on the intersection of the DSAH iso-Doppler curves $F_{ij}(\tau', \tau, \mu)$ and DSAH iso-Doppler-rate curves $\dot{F}_j(\tau, C)$. We assume that the flight trajectories of the receivers are smooth and that the receiver antenna beam patterns are focused on a region of interest where each pair of iso-Doppler $F_{ij}(\tau', \tau, \mu)$ and iso-Doppler-rate $\dot{F}_j(\tau, C)$ contours intersect at a single point within the region of interest. In other words, we assume that the only critical point within the region of interest is $z = z'$.

3.3. Determination of the weight and filter

The weight Q_{ij} and the filter B_{ij} can be determined with respect to various criteria [22]. Ideally, Q_{ij} and B_{ij} are chosen such that the leading-order contribution of the PSF of $\mathcal{K}_{ij}$ is the Dirac-delta function, i.e. $L_{ij}(z, z', \tau') \approx \delta(z - z')$. This choice of Q_{ij} and B_{ij} ensures that $\mathcal{K}_{ij}$ reconstructs the visible edges of the scene not only at the right location and orientation, but also with the correct strength [15, 22–24].

To determine the weight and the filter, we linearize $S_{ij}(\tau', \tau, z')$ around $z' = z$ and approximate

$$S_{ij}(\tau', \tau, z') - S_{ij}(\tau', \tau, z) \approx \nabla_z S_{ij}(\tau', \tau, z) \cdot (z' - z) \tag{54}$$

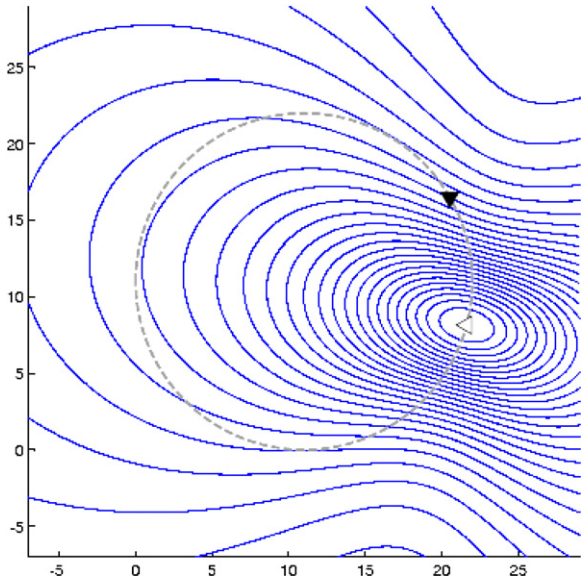

Figure 3. Iso-Doppler-rate contours $\dot{F}_j(\tau, C)$ for the DSAH Doppler-rate $f_1(-\pi/12, \mathbf{z})$. Two receivers are traversing a circular flight trajectory (dashed line) at the speed of 261 m s^{-1} over a flat topography. $\gamma_1(s) = \gamma_C(s)$ and $\gamma_2(s) = \gamma_C(s - \pi/4)$, respectively, where white and black triangles denote the positions of the two receivers at $s = \pi/6$, respectively. (See (52) and (73) for explicit formulas of $f_2(-\pi/12, \mathbf{z})$ and $\gamma_C(s)$, respectively.)

and

$$A_{ij}(\boldsymbol{z}', t, \tau', \tau) \approx A_{ij}(\boldsymbol{z}, t, \tau', \tau), \tag{55}$$

to write

$$L_{ij}(\boldsymbol{z}, \boldsymbol{z}', \tau') = \int \mathrm{e}^{-\mathrm{i}\, t\Xi_{ij}(\tau', \tau, \boldsymbol{z})\cdot(\boldsymbol{z}'-\boldsymbol{z})}\, Q_{ij}(\boldsymbol{z}, \tau', \tau) \frac{A_{ij}(\boldsymbol{z}, t, \tau', \tau)}{B_{ij}(\boldsymbol{z}, t, \tau', \tau)}\, |t|\, \mathrm{d}t\, \mathrm{d}\tau, \tag{56}$$

where

$$\Xi_{ij}(\tau', \tau, \boldsymbol{z}) = \omega_0[1 - (\widehat{\boldsymbol{\gamma}_j(\tau)} - \mathbf{z}) \cdot \dot{\boldsymbol{\gamma}}_j(\tau)/c_0]\nabla_{\boldsymbol{z}} S_{ij}(\tau', \tau, \boldsymbol{z}). \tag{57}$$

In (56), for each τ' and $\boldsymbol{z}$, we make the following change of variables:

$$(t, \tau) \to \boldsymbol{\xi}_{ij} = t\Xi_{ij}(\tau', \tau, \boldsymbol{z}). \tag{58}$$

Then

$$\left|\frac{\partial \boldsymbol{\xi}_{ij}}{\partial(t, \tau)}\right| = |t| \left|\det \begin{bmatrix} \Xi_{ij}(\tau', \tau, \boldsymbol{z}) \\ \partial_\tau \Xi_{ij}(\tau', \tau, \boldsymbol{z}) \end{bmatrix}\right|, \tag{59}$$

where det denotes matrix determinant.

Defining

$$\eta(\boldsymbol{z}, \tau', \tau) = |t| \left|\frac{\partial(t, \tau)}{\partial \boldsymbol{\xi}_{ij}}\right| = \left|\det \begin{bmatrix} \Xi_{ij}(\tau', \tau, \boldsymbol{z}) \\ \partial_\tau \Xi_{ij}(\tau', \tau, \boldsymbol{z}) \end{bmatrix}\right|^{-1}, \tag{60}$$

we rewrite (56) as

$$L_{ij}(\boldsymbol{z}, \boldsymbol{z}', \tau') = \int_{\Omega_{ij,\tau',\boldsymbol{z}}} \mathrm{e}^{-\mathrm{i}\, \boldsymbol{\xi}_{ij}\cdot(\boldsymbol{z}'-\boldsymbol{z})}\, Q_{ij}(\boldsymbol{z}, \tau', \boldsymbol{\xi}_{ij}) \eta(\boldsymbol{z}, \tau', \boldsymbol{\xi}_{ij}) \frac{A_{ij}(\boldsymbol{z}, \tau', \boldsymbol{\xi}_{ij})}{B_{ij}(\boldsymbol{z}, \tau', \boldsymbol{\xi}_{ij})}\, \mathrm{d}\boldsymbol{\xi}_{ij}, \tag{61}$$

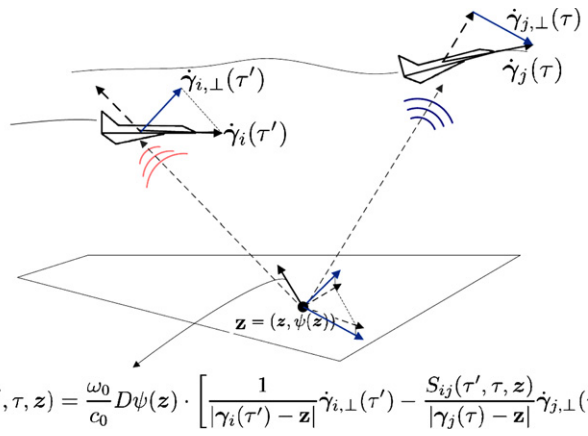

Figure 4. An illustration of the vector $\Xi_{ij}(\tau', \tau, z)$ in the data collection manifold $\Omega_{ij,z}$ for the flat topography, $\psi(z) = 0$. $\Xi_{ij}(\tau', \tau, z)$ is the projection of the difference of the scaled vectors $\dot{\gamma}_{i,\perp}(\tau')$ and $\dot{\gamma}_{j,\perp}(\tau)$ onto the tangent plane of the ground topography at $\mathbf{z}$. (See (67) for an explicit form of $\Xi_{ij}(\tau', \tau, z)$.)

where

$$Q_{ij}(z, \tau', \xi_{ij}) = Q_{ij}(z, \tau', \tau(\xi_{ij})) \tag{62}$$

$$A_{ij}(z, \tau', \xi_{ij}) = A_{ij}(z, t(\xi_{ij}), \tau', \tau(\xi_{ij})) \tag{63}$$

$$B_{ij}(z, \tau', \xi_{ij}) = B_{ij}(z, t(\xi_{ij}), \tau', \tau(\xi_{ij})) \tag{64}$$

$$\eta(z, \tau', \xi_{ij}) = \eta(z, \tau', \tau(\xi_{ij})). \tag{65}$$

In (61),

$$\Omega_{ij,\tau',z} = \{\xi_{ij} = t\Xi_{ij}(\tau', \tau, z) |\, A_{ij}(z, t, \tau', \tau) \neq 0, (t, \tau', \tau) \in (\mathbb{R}^+, \mathbb{R}, \mathbb{R})\}. \tag{66}$$

We refer to $\Omega_{ij,\tau',z}$ as the *partial data collection manifold* at (τ', z) obtained by the ith and jth receivers for a fixed τ' and refer to the union $\cup_{ij,\tau'}\Omega_{ij,\tau',z}$ as the *data collection manifold* at z and denote it by Ω_z. This set determines many of the properties of the image.

Using (57) and (20), we obtain

$$\Xi_{ij}(\tau', \tau, z) = \frac{\omega_0}{c_0} D\psi(z) \cdot \left[\frac{1}{|\gamma_i(\tau') - \mathbf{z}|} \dot{\gamma}_{i,\perp}(\tau') - \frac{S_{ij}(\tau', \tau, z)}{|\gamma_j(\tau) - \mathbf{z}|} \dot{\gamma}_{j,\perp}(\tau) \right], \tag{67}$$

where

$$D\psi(z) = \begin{bmatrix} 1 & 0 & \partial\psi(z)/\partial z_1 \\ 0 & 1 & \partial\psi(z)/\partial z_2 \end{bmatrix} \tag{68}$$

and $\dot{\gamma}_{i,\perp}(\tau')$, $\dot{\gamma}_{j,\perp}(\tau)$ are the projections of $\dot{\gamma}_i(\tau')$ and $\dot{\gamma}_j(\tau)$ onto the planes whose normal vectors are $(\widehat{\gamma_i(\tau') - \mathbf{z}})$ and $(\widehat{\gamma_j(\tau) - \mathbf{z}})$, respectively. For a detailed derivation of (67), see appendix B.

We show an illustration of the vector $\Xi_{ij}(\tau', \tau, z)$ in figure 4 for two receivers flying over a flat topography.

We choose the weight and the filter as follows:

$$Q_{ij}(z, \tau', \tau) = [\eta(z, \tau', \tau)]^{-1} = \left| \det \begin{bmatrix} \Xi_{ij}(\tau', \tau, z) \\ \partial_\tau \Xi_{ij}(\tau', \tau, z) \end{bmatrix} \right| \tag{69}$$

and

$$B_{ij}^{-1}(z,t,\tau',\tau,\mu) = A_{ij}^{-1}(z,t,\tau',\tau,\mu)\chi_{\Omega_{ij,\tau',z}}(z,t,\tau',\tau), \tag{70}$$

where $\chi_{\Omega_{ij,\tau',z}}$ is a smooth cut-off function equal to one in the interior of $\Omega_{ij,\tau',z}$ and zero in the exterior of $\Omega_{ij,\tau',z}$. To avoid instability, $B_{ij}(z,t,\tau',\tau,\mu)$ can be modified to

$$B_{ij}^{-1}(z,t,\tau',\tau,\mu) = \frac{\overline{A_{ij}(z,t,\tau',\tau,\mu)}\,\chi_{\Omega_{ij,\tau',z}}(z,t,\tau',\tau)}{|A_{ij}(z,t,\tau',\tau,\mu)|^2+\sigma^2} \tag{71}$$

where σ^2 is a small positive constant.

Note that we choose the filter to compensate for the terms involving antenna beam patterns and geometric spreading functions and the weight to perform proper interpolation in the phase space going from (t,τ) to $\boldsymbol{\xi}_{ij}$ coordinates. These choices make the leading-order term of $L_{ij}(z,z',\tau')$ in (61) to be the Dirac-delta function.

Substituting (69) and (70) into (61) and the result into (37), we obtain

$$\tilde{R}_\rho(z) = \sum_{ij}\mathcal{K}_{ij}[\mathcal{F}_{ij}[R_\rho]](z) \approx \sum_{ij}\int_{\Omega_{ij,\tau',z}} \mathrm{e}^{-\mathrm{i}\boldsymbol{\xi}_{ij}\cdot(z'-z)}\,R_\rho(z')\,\mathrm{d}z'\,\mathrm{d}\boldsymbol{\xi}_{ij}\,\mathrm{d}\tau'. \tag{72}$$

Equation (72) shows that the image $\tilde{R}_\rho$ is a bandlimited version of R_ρ whose bandwidth is determined by the data collection manifold Ω_z, which describes the resolution of the reconstructed image $\tilde{R}_\rho$ at z. The larger the data collection manifold, the better the resolution of the reconstructed image.

Microlocal analysis of (72) tell us that an edge at point z is visible if the direction $\boldsymbol{n}_z$ normal to the edge is contained in Ω_z [15, 22–24]. Consequently, an edge at point z with $\boldsymbol{n}_z$ normal to edge is visible if there exists i,j,τ',τ such that $\boldsymbol{\xi}_{ij}$ is parallel to $\boldsymbol{n}_z$. Furthermore, the bandwidth contribution of $\boldsymbol{\xi}_{ij} = t\boldsymbol{\Xi}_{ij}(\tau',\tau,z)$ to a visible edge at z is given by $L_\phi|\boldsymbol{\Xi}_{ij}(\tau',\tau,z)|$, where L_ϕ denotes the length of the support of $\phi(t)$. Thus, the longer the support of $\phi(t)$, the larger the magnitude of $\boldsymbol{\xi}_{ij}$, giving rise to sharper reconstructed edges perpendicular to $\boldsymbol{\xi}_{ij}$, $i,j = 1,\ldots,N$. Additionally, the higher, ω_0, the frequency of the transmitted signal, the larger the magnitude of $\boldsymbol{\xi}_{ij}$, contributing to higher image resolution.

Equation (72) shows that irrespective of the choice of the weight and filter, the backprojection operator recovers the visible edges of the scene radiance at the right location for given ith and jth receivers and a fixed τ'. With the choice of the weight and filter given in (69) and (70), respectively, the resulting image formation algorithm recovers the visible edges of the scene radiance not only at the correct location and orientation, but also at the correct strength.

4. Numerical simulations

We conducted two sets of numerical simulations. In the first set of simulations, we numerically studied the PSF of the imaging operator under different scenarios and numerically demonstrated the theoretical results described in subsection 3.3. In the second set of simulations, we demonstrated the performance of our imaging method for a multiple-point-target model.

We considered a scene of size $[0,22]\times[0,22]\,\mathrm{km}^2$ with flat topography. The scene was discretized by 128×128 pixels, where $[0,0,0]$ km and $[22,22,0]$ km correspond to the pixels $(1,1)$ and $(128,128)$, respectively.

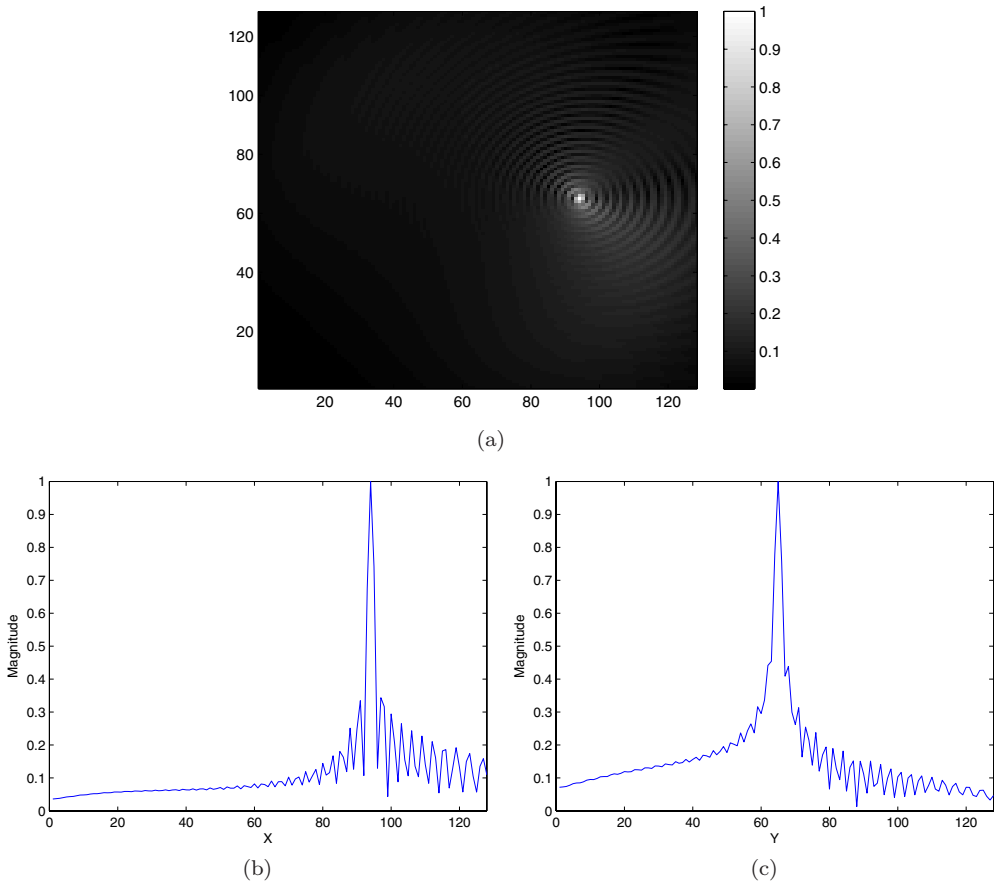

Figure 5. (a) The PSF of the DSAH imaging method at $(16, 11, 0)$ km along with (b) its X profile and (c) Y profile, for a cooperative transmitter located at $\mathbf{y}_0$, transmitting a CW waveform at $f_0 = 0.4$ MHz; and two receivers traversing circular trajectories, $\gamma_1(s)$ and $\gamma_2(s)$. The length of the support of the windowing function is $L_\phi = 3.657$ s.

In all the numerical experiments, we used two airborne receivers and a single, stationary transmitter operating either cooperatively or non-cooperatively. We assumed that both the receiver and transmitter antennas were isotropic. We assumed that the transmitter was located at $\mathbf{y}_0 = (0, 0, 6.5)$ km and the receivers were traversing the circular trajectory given by

$$\gamma_C(s) = (11 + 11\cos(s), 11 + 11\sin(s), 6.5) \text{ km}. \tag{73}$$

Let $\gamma_1(s)$ and $\gamma_2(s)$ denote the trajectories of the two receivers. We set $\gamma_1(s) = \gamma_C(s)$ and $\gamma_2(s) = \gamma_1\big(s - \frac{\pi}{6}\big)$. Note that the variable s in γ_C is equal to $\frac{V}{R}t$, where V is the speed of the receiver, and R is the radius of the circular trajectory. We set the speed of the two receivers to 261 m s^{-1}. We chose the sampling rate of τ to be 1.9335 Hz so as to uniformly sample the circular trajectory with 512 points.

For all the numerical experiments, we used (3) to generate the data and chose the windowing function ϕ in (6) to be a Hanning function. Since we used complex data for image formation, the reconstructed images may be complex even though the target reflectivity

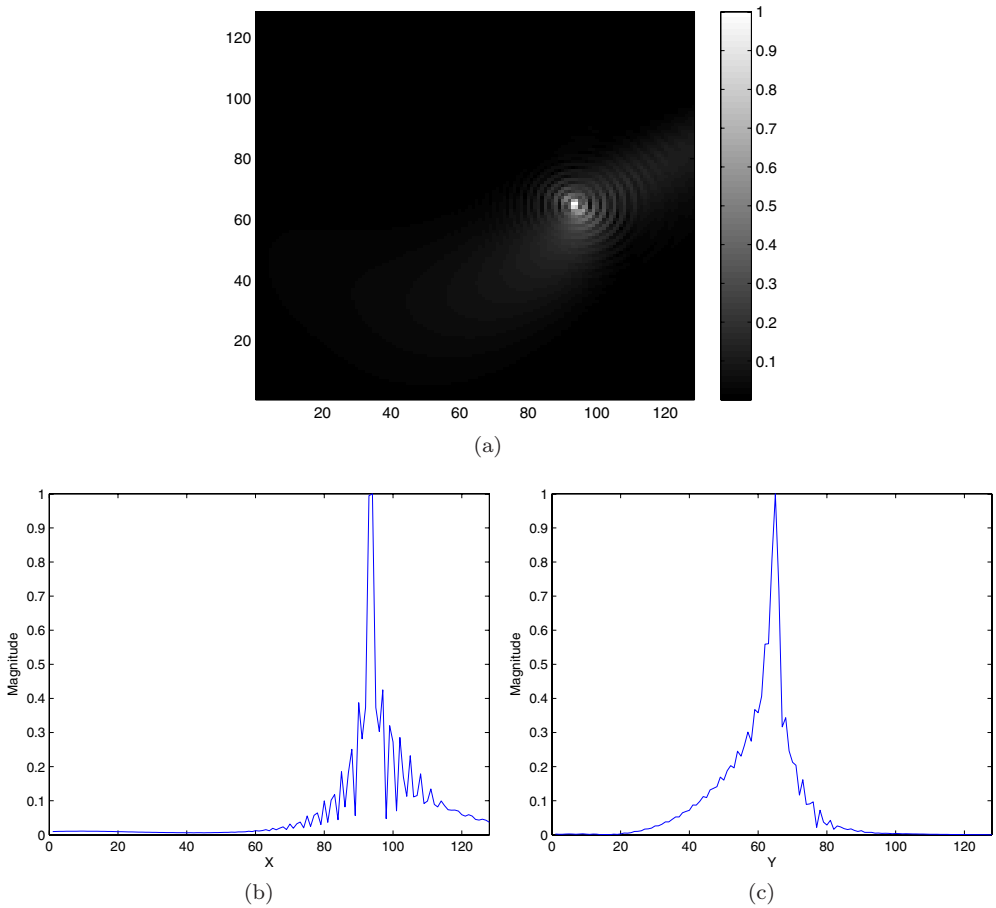

Figure 6. (a) The PSF of the DSAH imaging method at $(16, 11, 0)$ km along with (b) its X profile and (c) Y profile, for a cooperative transmitter located at $\mathbf{y}_0$, transmitting a CW waveform at $f_0 = 0.4$ MHz; and two receivers traversing circular trajectories, $\boldsymbol{\gamma}_1(s)$ and $\boldsymbol{\gamma}_2(s)$. The length of the support of the windowing function is $L_\phi = 14.629$ s.

is assumed to be real. Therefore, we display the magnitude images in the numerical simulation results.

We performed image reconstruction for each τ' and coherently superimposed the reconstructed images obtained over a range of τ'.

4.1. Numerical analysis of PSF

We placed a point target with unit reflectivity at $[16, 11, 0]$ km. Note that this position corresponds to the $(65, 94)$th pixel in the reconstructed scene.

We performed numerical simulations to demonstrate the impact of L_ϕ, the length of the support of $\phi(t)$; $f_0 = \omega_0/2\pi$, the frequency of the transmitted waveform and the range of τ' on the PSF of the imaging operator. We reconstructed the PSF with the following variables: (1) $f_0 = 0.4$ MHz, $L_\phi = 3.657$ s; (2) $f_0 = 0.4$ MHz, $L_\phi = 14.629$ s; (3) $f_0 = 4$ MHz, $L_\phi = 3.657$ s; (4) $\tau' \in [0, 248.258]$ s with the sampling period 16.551 s , $L_\phi = 0.0853$ s and

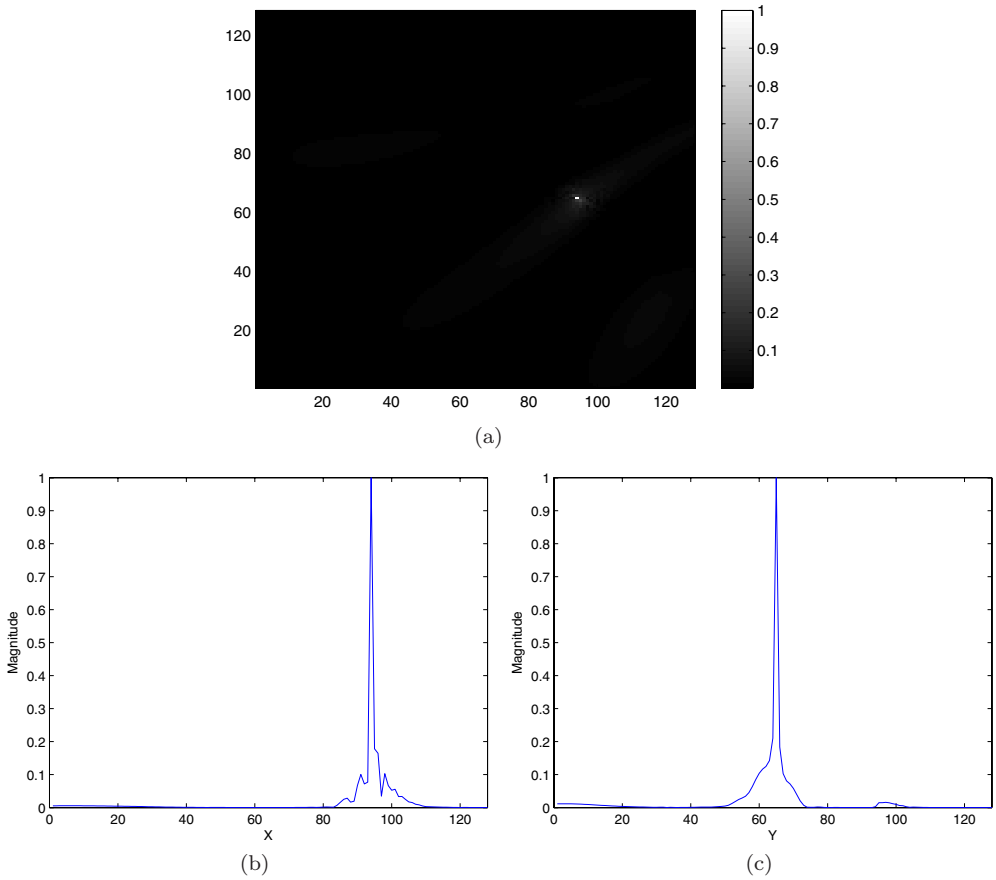

Figure 7. (a) The PSF of the DSAH imaging method at (16, 11, 0) km along with (b) its X profile and (c) Y profile, for a cooperative transmitter located at $\mathbf{y}_0$, transmitting a CW waveform at $f_0 = 4$ MHz; and two receivers traversing circular trajectories, $\boldsymbol{\gamma}_1(s)$ and $\boldsymbol{\gamma}_2(s)$. The length of the support of the windowing function is $L_\phi = 3.657$ s.

$f_0 = 800$ MHz. For the first three cases, we assumed that the transmitter was cooperative and reconstructed the PSF using $\tau' = 0$ s. For the fourth case, we reconstructed the PSF for both the cooperative and non-cooperative cases. We used 16 τ' values uniformly spaced in [0, 248.258] s.

Figures 5–7 show the reconstructed PSFs along with their profiles in X and Y directions for the first three cases.

As can be seen in figures 5 and 6, the quality of the PSF improves as the length of the support of the windowing function increases from 3.657 s to 14.629 s because of a larger data collection manifold. Comparing the profiles of the PSFs in both cases, we see that the level of the sidelobes of the PSF decreases as the support of windowing function gets longer. This, in turn, results in an increase in the image contrast.

Comparing figure 7 with figures 5 and 6, we see that the increase in the frequency of the transmitted waveform from 0.4 MHz to 4 MHz results in a clear improvement of the PSF as indicated by theory. We observe significant improvements in the resolution and the suppression of the sidelobes of the PSF in figures 7(b) and (c).

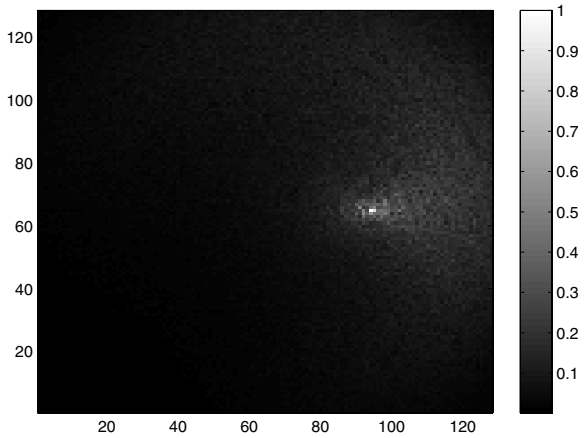

Figure 8. The PSF at [16, 11, 0] km with 16 τ' values uniformly spaced in [0, 248.258] s using a single cooperative transmitter located at $\mathbf{y}_0$ and two receivers traversing the circular flight trajectories $\gamma_1(s)$ and $\gamma_2(s)$, as shown in figure 11.

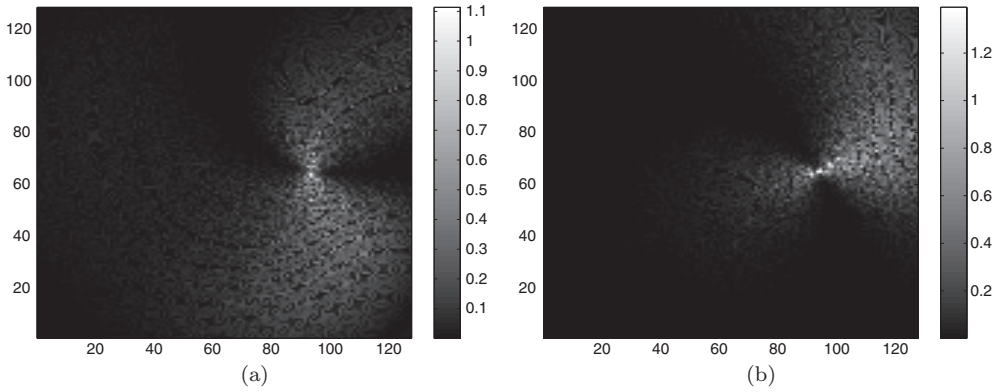

Figure 9. The PSFs using the vectors in the partial data collection manifolds (a) $\Omega_{12,\tau'=33.1011\text{ s}}$ (corresponding to $s = \pi/4$), and (b) $\Omega_{12,\tau'=165.5054\text{ s}}$ (corresponding to $s = 1.25\pi$), with a single cooperative transmitter located at $\mathbf{y}_0$ as shown in figure 11 and two receivers traversing circular flight trajectories $\gamma_1(s)$ and $\gamma_2(s)$ shown in figure 11.

To demonstrate the effect of the superposition of images reconstructed for each τ', we reconstructed the PSF for a range of τ' values. For this simulation, we used both cooperative and non-cooperative transmitters with the parameters described above. Figure 8 shows the reconstructed PSF, which is the superposition of the images obtained for 16 different τ' values uniformly spaced in [0, 248.258] s for a cooperative transmitter. To show the effect of the superposition of the reconstructed images and the value of τ', we present the reconstructed images corresponding to two different values of τ' in figure 9(a) and figure 9(b).

As expected, since the partial data collection manifold $\Omega_{12,\tau',z}$ for a fixed τ' is significantly smaller than $\cup_{\tau'}\Omega_{12,\tau',z}$, the resolution of the images in figure 9 is poorer than that of the superimposed image in figure 8.

For the case of non-cooperative transmitters, we assumed that the scene was illuminated by an isotropic antenna and set $\tilde{R}_T = 1$. Furthermore, we set $|\mathbf{T} - \mathbf{z}|^2 = 1$ for all $\mathbf{z} \in \mathbb{R}^3$

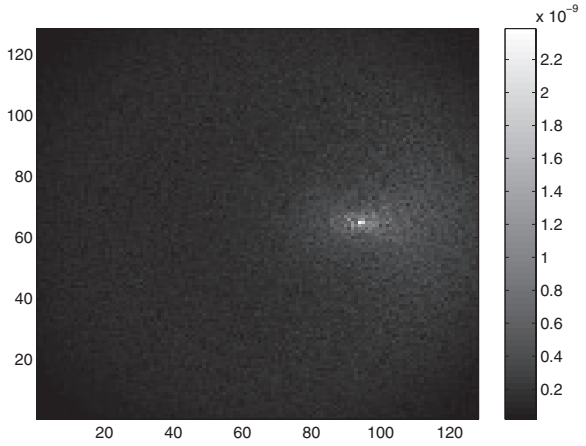

Figure 10. The reconstructed image for a point target with 16 τ' values uniformly spaced in [0, 248.258] s using a single non-cooperative transmitter located at $\mathbf{y}_0$ and two receivers traversing the circular flight trajectories $\gamma_1(s)$ and $\gamma_2(s)$ shown in figure 11.

in G_{ij} for the image reconstruction. This can be interpreted as an uninformative prior on the transmitter antenna beam patterns and the transmitter-related geometric spreading factors.

The reconstructed PSF for the case of a single non-cooperative transmitter is presented in figure 10. Without the transmitter-related geometric spreading factors in the reconstruction formula, the strength of the target appears weak because of the range-dependent attenuation. If *a priori* information on the rough location of the transmitters is available, this range-dependent attenuation can be easily corrected by rescaling the correlated received signal.

4.2. Numerical simulations for multiple-point targets

In accordance with the incoherent field approximation, we used the following multiple-point-target model for the scene reflectivity

$$\rho(\boldsymbol{z}) = \sum_{l=1}^{L} g_l \delta(\boldsymbol{z} - \boldsymbol{z}_l), \tag{74}$$

where $g_l, l = 1, \ldots, L$, are independent Gaussian random variables with mean μ_l and variance σ_l^2. The corresponding scene radiance is given by

$$R_\rho(\boldsymbol{z}) = E[\rho(\boldsymbol{z})\rho^*(\boldsymbol{z})] = \sum_{l} \left(\mu_l^2 + \sigma_l^2\right)\sigma(\boldsymbol{z} - \boldsymbol{z}_l). \tag{75}$$

In our simulations, we considered a deterministic reflectivity and set $\sigma_l^2 = 1$. We used $L = 9$ and approximated the Dirac-delta functions in (75) by square target reflectors of size $344 \times 344\,\mathrm{m}^2$, each having a unit reflectivity, i.e. $\mu_l = 1$, $l = 1, \ldots, 9$. Figures 11(a) and (b) show the scene with targets, receiver trajectories and the transmitter antenna location.

4.2.1. Cooperative transmitters. For the case of a cooperative transmitter, the reconstructed image is shown in figure 12. The two images corresponding to the fixed τ' values are shown in figures 13(a) and (b). As expected, because of a smaller data collection manifold, the

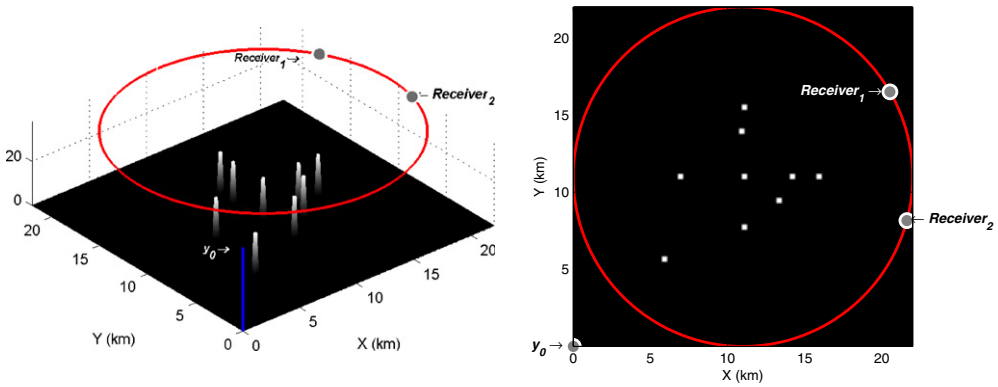

(a) (b)

Figure 11. (a) 3D and (b) 2D views of the scene with multiple-point targets, illuminated by a single transmitter located at $\mathbf{y}_0 = (0, 0, 6.5)$ km and the circular receiver trajectory $\gamma_C(s) = (11 + 11\cos(s), 11 + 11\sin(s), 6.5)$ km, as shown by the circle. At a certain time instant, two receivers are located at the positions shown in the figure.

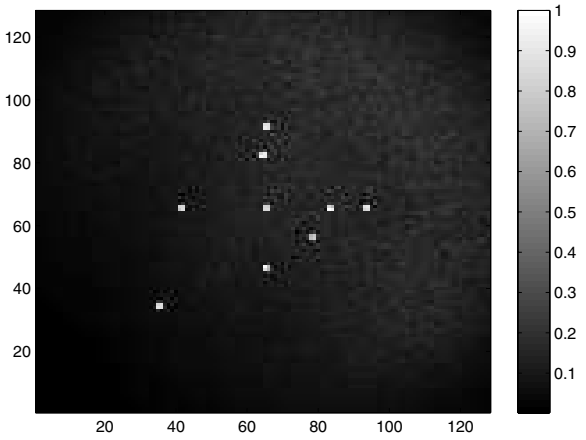

Figure 12. The reconstructed image for multiple-point targets with 16 τ' values uniformly spaced in [0, 248.258] s using a single cooperative transmitter located at $\mathbf{y}_0$ and two receivers traversing the circular flight trajectories $\gamma_1(s)$ and $\gamma_2(s)$ as shown in figure 11.

resolution of these images is poorer than that of the image obtained by superposition of all the images reconstructed for a range of τ' values, $\tau' \in [0, 248.258]$ s, as shown in figure 12. We observe that some of the targets do not appear as sharp as the ones in figure 12.

4.2.2. Non-cooperative transmitters. Figure 14 shows the reconstructed image for multiple-point targets using a non-cooperative transmitter. Since the location of the transmitter was assumed to be unknown, the received signal was not compensated for the transmitter related geometric spreading factors. As a result, the scatterers closer to the transmitter appear brighter in the reconstructed image than those that are further away from the transmitter.

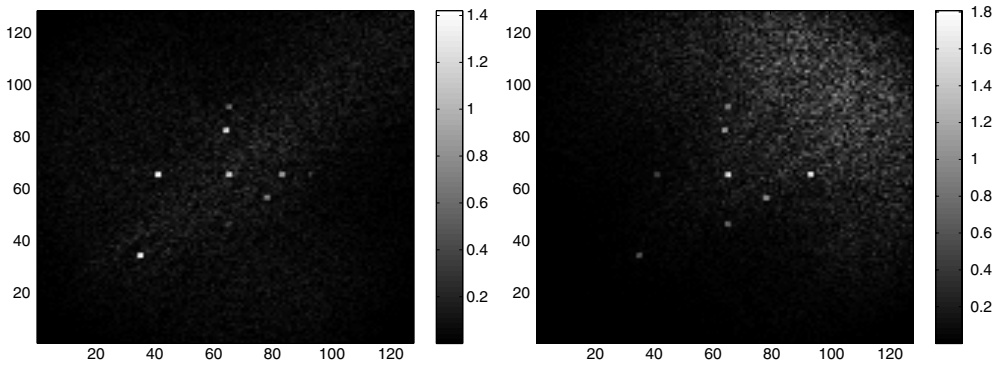

Figure 13. The images reconstructed for multiple-point targets using the vectors in the partial data collection manifolds (a) $\Omega_{12,\tau'=33.1011\text{ s}}$ (corresponding to $s = \pi/4$), and (b) $\Omega_{12,\tau'=165.5054\text{ s}}$ (corresponding to $s = 1.25\pi$), with a single cooperative transmitter located at $\mathbf{y}_0$ and two receivers traversing circular flight trajectories $\boldsymbol{\gamma}_1(s)$ and $\boldsymbol{\gamma}_2(s)$ as shown in figure 11.

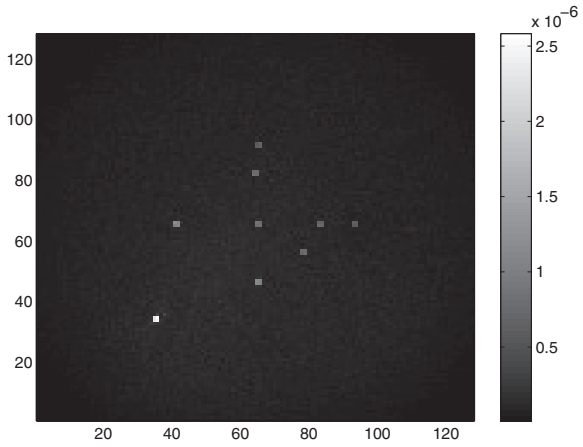

Figure 14. The reconstructed image for multiple-point targets with 16 τ' values uniformly sampled in [0, 248.258] s using a single non-cooperative transmitter located at $\mathbf{y}_0$ and two receivers traversing the circular flight trajectories $\boldsymbol{\gamma}_1(s)$ and $\boldsymbol{\gamma}_2(s)$ as shown in figure 11.

5. Conclusion

We developed a novel image formation method for passive SAR that uses transmitters of opportunity with single-frequency or ultra-narrowband waveforms and receivers traversing arbitrary flight trajectories. The method is based on the windowed, filtered, scaled and translated correlation of the received signals at different (or the same) receiver and weighted backprojection of the resulting correlated signal. Such preprocessing of the received signal removes the transmitter-related terms from the phase of the resulting forward model, allowing us to perform backprojection without knowledge of the transmitter locations. For non-cooperative transmitters of opportunity, we assumed that the location and antenna beam patterns of the transmitters are unknown and treat antenna beam patterns as random processes

with known second-order statistics. For cooperative sources of opportunity, we assumed that the location and antenna beam patterns of the transmitters are known.

The windowed, filtered, scaled and translated correlations of the received signal result in the projection of the ground radiance onto the curves defined by the Doppler hitchhiker scale factor. Next we used microlocal analysis to recover ground radiance from its projections via weighted backprojection. The analysis of the point spread function of the imaging operator shows that the singularities of the scene radiance that are reconstructed are those that are at the intersection of the curves defined by the Doppler hitchhiker scale factor and hitchhiker iso-Doppler-rate curves. The weighted backprojection algorithm puts the visible edges of the scene radiance at the correct location, and under appropriate conditions, with correct strength.

The analysis of the Fourier space data collection manifold shows that the resolution of the reconstructed image depends on the frequency of the transmitter, the length of the support of the windowing function, the Doppler hitchhiker scale factor and the range of the τ' variables. The numerical simulations demonstrate the performance of the reconstruction algorithm and verify the theoretical results.

We described our imaging algorithm for a single, stationary transmitter. However, the method can be easily extended to multiple mobile or stationary transmitters by simply integrating the received signal model over all transmitter locations similar to our work in [6]. Following the methodology introduced in [22, 25–27], it can be shown that correlation of scaled and delayed measurements is an optimal detection scheme for a point target in the presence of additive white Gaussian noise. This result as well as imaging in the presence of more general noise models and performance analysis will be described in our future work [28].

Although we presented our approach specifically for passive synthetic aperture radar, our method is also applicable to other passive imaging problems, such as passive geophysical or acoustic imaging.

Acknowledgments

This work is supported by the Air Force Office of Scientific Research[3] (AFOSR) under the agreement FA9550-07-1-0363 and by the National Science Foundation (NSF) under Grant No. CCF-08030672.

Appendix A.

Substituting (20) into

$$\partial_\tau(\omega_0 t[1-(\widehat{\gamma_j(\tau)}-\mathbf{z})\cdot\dot{\gamma}_j(\tau)/c_0][S_{ij}(\tau',\tau,z')-S_{ij}(\tau',\tau,z)])=0, \tag{A.1}$$

we reduce (A.1) to

$$-\omega_0 t[1-(\widehat{\gamma_i(\tau')}-\mathbf{z}')\cdot\dot{\gamma}_i(\tau')/c_0]\,\underbrace{\partial_\tau\left[\frac{1-(\widehat{\gamma_j(\tau)}-\mathbf{z})\cdot\dot{\gamma}_j(\tau)/c_0}{1-(\widehat{\gamma_j(\tau)}-\mathbf{z}')\cdot\dot{\gamma}_j(\tau)/c_0}\right]}_{\Delta}=0. \tag{A.2}$$

[4] Consequently the US Government is authorized to reproduce and distribute reprints for Governmental purposes notwithstanding any copyright notation thereon. The views and conclusions contained herein are those of the authors and should not be interpreted as necessarily representing the official policies or endorsements, either expressed or implied, of the Air Force Research Laboratory or the US Government.

We now express Δ as

$$\partial_\tau\left[\frac{1-(\widehat{\gamma_j(\tau)-\mathbf{z}})\cdot\dot{\gamma}_j(\tau)/c_0}{1-(\widehat{\gamma_j(\tau)-\mathbf{z}'})\cdot\dot{\gamma}_j(\tau)/c_0}\right]$$
$$= -\frac{1-(\widehat{\gamma_j(\tau)-\mathbf{z}})\cdot\dot{\gamma}_j(\tau)/c_0}{[1-(\widehat{\gamma_j(\tau)-\mathbf{z}'})\cdot\dot{\gamma}_j(\tau)/c_0]^2}\times\partial_\tau[1-(\widehat{\gamma_j(\tau)-\mathbf{z}'})\cdot\dot{\gamma}_j(\tau)/c_0]$$
$$+\frac{1}{1-(\widehat{\gamma_j(\tau)-\mathbf{z}'})\cdot\dot{\gamma}_j(\tau)/c_0}\times\partial_\tau[1-(\widehat{\gamma_j(\tau)-\mathbf{z}})\cdot\dot{\gamma}_j(\tau)/c_0]. \tag{A.3}$$

Introducing (A.3) into (A.2), we obtain

$$\frac{\partial_\tau[1-(\widehat{\gamma_j(\tau)-\mathbf{z}})\cdot\dot{\gamma}_j(\tau)/c_0]}{1-(\widehat{\gamma_j(\tau)-\mathbf{z}})\cdot\dot{\gamma}_j(\tau)/c_0}=\frac{\partial_\tau[1-(\widehat{\gamma_j(\tau)-\mathbf{z}'})\cdot\dot{\gamma}_j(\tau)/c_0]}{1-(\widehat{\gamma_j(\tau)-\mathbf{z}'})\cdot\dot{\gamma}_j(\tau)/c_0}. \tag{A.4}$$

Let us focus on the numerators on both sides of (A.4). Using the notations $\gamma_j = \left[\gamma_j^1,\gamma_j^2,\gamma_j^3\right]^T$ and $\dot{\gamma}_j=\left[\dot{\gamma}_j^1,\dot{\gamma}_j^2,\dot{\gamma}_j^3\right]^T$, the partial derivative of the numerator on the left-hand side of (A.4) with respect to τ can be expressed as

$$\partial_\tau[1-(\widehat{\gamma_j(\tau)-\mathbf{z}})\cdot\dot{\gamma}_j(\tau)/c_0]=\partial_\tau\frac{-1}{c_0\,|\gamma_j(\tau)-\mathbf{z}|}\left[\left(\gamma_j^1(\tau)-z_1\right)\dot{\gamma}_j^1(\tau)\right.$$
$$\left.+\left(\gamma_j^2(\tau)-z_2\right)\dot{\gamma}_j^2(\tau)+\left(\gamma_j^3(\tau)-z_3\right)\dot{\gamma}_j^3(\tau)\right]$$
$$=\left[\frac{1}{c_0\,|\gamma_j(\tau)-\mathbf{z}|^2}\frac{\gamma_j(\tau)-\mathbf{z}}{|\gamma_j(\tau)-\mathbf{z}|}\cdot\dot{\gamma}_j(\tau)\right][(\gamma_j(\tau)-\mathbf{z})\cdot\dot{\gamma}_j(\tau)]$$
$$-\frac{1}{c_0\,|\gamma_j(\tau)-\mathbf{z}|}\left[\left(\dot{\gamma}_j^1(\tau)\right)^2+\left(\gamma_j^1(\tau)-z_1\right)\ddot{\gamma}_j^1(\tau)+\left(\dot{\gamma}_j^2(\tau)\right)^2\right.$$
$$\left.+\left(\gamma_j^2(\tau)-z_2\right)\ddot{\gamma}_j^2(\tau)+\left(\dot{\gamma}_j^3(\tau)\right)^2+\left(\gamma_j^3(\tau)-z_3\right)\ddot{\gamma}_j^3(\tau)\right]$$
$$=\frac{1}{c_0\,|\gamma_j(\tau)-\mathbf{z}|}[(\widehat{\gamma_j(\tau)-\mathbf{z}})\cdot\dot{\gamma}_j(\tau)]^2$$
$$-\frac{1}{c_0\,|\gamma_j(\tau)-\mathbf{z}|}[|\dot{\gamma}_j(\tau)|^2+(\gamma_j(\tau)-\mathbf{z})\cdot\ddot{\gamma}_j(\tau)]$$
$$=\frac{-1}{c_0}\left[\frac{1}{|\gamma_j(\tau)-\mathbf{z}|}[|\dot{\gamma}_j(\tau)|^2-((\widehat{\gamma_j(\tau)-\mathbf{z}})\cdot\dot{\gamma}_j(\tau))^2]+(\widehat{\gamma_j(\tau)-\mathbf{z}})\cdot\ddot{\gamma}_j(\tau)\right]$$
$$=\frac{-1}{c_0}\left[\frac{1}{|\gamma_j(\tau)-\mathbf{z}|}|\dot{\gamma}_{j,\perp}(\tau,\mathbf{z})|^2+\underbrace{(\widehat{\gamma_j(\tau)-\mathbf{z}})\cdot\ddot{\gamma}_j(\tau)}_{a_j(\tau,\mathbf{z})}\right] \tag{A.5}$$

where

$$\dot{\gamma}_{j,\perp}(\tau,\mathbf{z})=\dot{\gamma}_j(\tau)-(\widehat{\gamma_j(\tau)-\mathbf{z}})((\widehat{\gamma_j(\tau)-\mathbf{z}})\cdot\dot{\gamma}_j(\tau)) \tag{A.6}$$

denotes the projection of the receiver velocity $\dot{\gamma}_j(\tau)$ onto the plane whose normal direction is along $\widehat{\gamma_j(\tau)-\mathbf{z}}$ and $a_j(\tau,\mathbf{z})$ denotes the projection of the receiver acceleration $\ddot{\gamma}_j(\tau)$ along $\widehat{\gamma_j(\tau)-\mathbf{z}}$. We see that the summation of the two terms in the square bracket of (A.5) is the total radial acceleration of the jth receiver evaluated at τ. We denote these two terms by $a_j^{\sum}(\tau,\mathbf{z})$, i.e.

$$a_j^{\sum}(\tau,\mathbf{z})=\frac{1}{|\gamma_j(\tau)-\mathbf{z}|}|\dot{\gamma}_{j,\perp}(\tau,\mathbf{z})|^2+(\widehat{\gamma_j(\tau)-\mathbf{z}})\cdot\ddot{\gamma}_j(\tau). \tag{A.7}$$

Introducing (A.5) into (A.4), we obtain

$$\frac{a_j^{\sum}(\tau, \mathbf{z})}{1 - (\widehat{\gamma_j(\tau) - \mathbf{z}}) \cdot \dot{\gamma}_j(\tau)/c_0} = \frac{a_j^{\sum}(\tau, \mathbf{z}')}{1 - (\widehat{\gamma_j(\tau) - \mathbf{z}'}) \cdot \dot{\gamma}_j(\tau)/c_0}. \tag{A.8}$$

Appendix B.

Introducing (20) in (57),

$$\Xi_{ij}(\tau', \tau, z) = \omega_0[1 - (\widehat{\gamma_j(\tau) - \mathbf{z}}) \cdot \dot{\gamma}_j(\tau)/c_0]\nabla_z S_{ij}(\tau', \tau, z), \tag{B.1}$$

we obtain

$$\begin{aligned}\Xi_{ij}(\tau', \tau, z) = \omega_0 \Bigg[& \nabla_{\mathbf{z}}(1 - (\widehat{\gamma_i(\tau') - \mathbf{z}}) \cdot \dot{\gamma}_i(\tau')/c_0) \\ & - \frac{1 - (\widehat{\gamma_i(\tau') - \mathbf{z}}) \cdot \dot{\gamma}_i(\tau')/c_0}{1 - (\widehat{\gamma_j(\tau) - \mathbf{z}}) \cdot \dot{\gamma}_j(\tau)/c_0} \cdot \nabla_{\mathbf{z}}(1 - (\widehat{\gamma_j(\tau) - \mathbf{z}}) \cdot \dot{\gamma}_j(\tau)/c_0) \Bigg]\end{aligned} \tag{B.2}$$

where $\nabla_{\mathbf{z}} = \left[\partial_{z_1}, \partial_{z_2}\right]^T$.

Defining $\mu = S_{ij}(\tau', \tau, z)$, (B.2) can be expressed as

$$\begin{aligned}\Xi(\tau', \tau, z) &= \omega_0[\nabla_{\mathbf{z}}(1 - (\widehat{\gamma_i(\tau') - \mathbf{z}}) \cdot \dot{\gamma}_i(\tau')/c_0) \\ &\quad - \mu\nabla_{\mathbf{z}}(1 - (\widehat{\gamma_j(\tau) - \mathbf{z}}) \cdot \dot{\gamma}_j(\tau)/c_0)] \\ &= \frac{\omega_0}{c_0}[\mu\nabla_{\mathbf{z}}(\widehat{\gamma_j(\tau) - \mathbf{z}} \cdot \dot{\gamma}_j(\tau)) - \nabla_{\mathbf{z}}(\widehat{\gamma_i(\tau') - \mathbf{z}}) \cdot \dot{\gamma}_i(\tau')].\end{aligned} \tag{B.3}$$

Let us write

$$\begin{aligned}(\widehat{\gamma_i(\tau') - \mathbf{z}}) \cdot \dot{\gamma}_i(\tau') = \frac{1}{|\gamma_i(\tau') - \mathbf{z}|}\big[&\big(\gamma_i^1(\tau') - z_1\big)\dot{\gamma}_i^1(\tau') \\ &+ \big(\gamma_i^2(\tau') - z_2\big)\dot{\gamma}_i^2(\tau') + \big(\gamma_i^3(\tau') - \psi(z_1, z_2)\big)\dot{\gamma}_i^3(\tau')\big]\end{aligned} \tag{B.4}$$

where $\gamma_i = \left[\gamma_i^1, \gamma_i^2, \gamma_i^3\right]^T$ and $\dot{\gamma}_i = \left[\dot{\gamma}_i^1, \dot{\gamma}_i^2, \dot{\gamma}_i^3\right]^T$. Calculating the first-order partial derivative of (B.4) with respect to z_1, we obtain

$$\begin{aligned}\frac{\partial(\widehat{\gamma_i(\tau') - \mathbf{z}}) \cdot \dot{\gamma}_i(\tau')}{\partial z_1} = &\frac{-1}{|\gamma_i(\tau') - \mathbf{z}|^2} \\ &\times \left[\frac{-\big(\gamma_i^1(\tau') - z_1\big) - \frac{\partial\psi}{\partial z_1}\big(\gamma_i^3(\tau') - \psi(z_1, z_2)\big)}{|\gamma_i(\tau') - \mathbf{z}|}((\gamma_i(\tau') - \mathbf{z}) \cdot \dot{\gamma}_i(\tau'))\right] \\ &+ \frac{1}{|\gamma_i(\tau') - \mathbf{z}|}\left[-\dot{\gamma}_i^1(\tau') - \frac{\partial\psi}{\partial z_1}\dot{\gamma}_i^3(\tau')\right].\end{aligned} \tag{B.5}$$

Similarly, we obtain the partial differential of (B.4) with respect to z_2.

Let

$$D\psi(z) = \begin{bmatrix}1 & 0 & \partial\psi(z)/\partial z_1 \\ 0 & 1 & \partial\psi(z)/\partial z_2\end{bmatrix}. \tag{B.6}$$

Then, using (B.5), we have

$$\begin{aligned}&\nabla_{\mathbf{z}}(\widehat{\gamma_i(\tau') - \mathbf{z}}) \cdot \dot{\gamma}_i(\tau') \\ &\quad = \frac{-1}{|\gamma_i(\tau') - \mathbf{z}|}D\psi(z) \cdot [\underbrace{\dot{\gamma}_i(\tau') - (\widehat{\gamma_i(\tau') - \mathbf{z}})((\widehat{\gamma_i(\tau') - \mathbf{z}}) \cdot \dot{\gamma}_i(\tau'))}_{\dot{\gamma}_{i,\perp}(\tau')}].\end{aligned} \tag{B.7}$$

Similarly, we obtain

$$\nabla_{\mathbf{z}}(\widehat{\boldsymbol{\gamma}_j(\tau) - \mathbf{z}}) \cdot \dot{\boldsymbol{\gamma}}_j(\tau) = \frac{-1}{|\boldsymbol{\gamma}_j(\tau) - \mathbf{z}|} D\psi(\boldsymbol{z}) \cdot [\underbrace{\dot{\boldsymbol{\gamma}}_j(\tau) - (\widehat{\boldsymbol{\gamma}_j(\tau) - \mathbf{z}})((\widehat{\boldsymbol{\gamma}_j(\tau) - \mathbf{z}}) \cdot \dot{\boldsymbol{\gamma}}_j(\tau))}_{\dot{\boldsymbol{\gamma}}_{j,\perp}(\tau)}]. \tag{B.8}$$

Note that $\dot{\boldsymbol{\gamma}}_{i,\perp}(\tau')$ and $\dot{\boldsymbol{\gamma}}_{j,\perp}(\tau)$ are the projections of the receiver velocities $\dot{\boldsymbol{\gamma}}_i(\tau')$ and $\dot{\boldsymbol{\gamma}}_j(\tau)$ onto the planes perpendicular to the directions $\widehat{\boldsymbol{\gamma}_i(\tau') - \mathbf{z}}$ and $\widehat{\boldsymbol{\gamma}_j(\tau) - \mathbf{z}}$, respectively.

Substituting (B.7) and (B.8) into (B.3), we obtain

$$\boldsymbol{\Xi}_{ij}(\tau', \tau, \boldsymbol{z}) = \frac{\omega_0}{c_0} D\psi(\boldsymbol{z}) \cdot \left[\frac{1}{|\boldsymbol{\gamma}_i(\tau') - \mathbf{z}|} \dot{\boldsymbol{\gamma}}_{i,\perp}(\tau') - \frac{\mu}{|\boldsymbol{\gamma}_j(\tau) - \mathbf{z}|} \dot{\boldsymbol{\gamma}}_{j,\perp}(\tau) \right]. \tag{B.9}$$

References

[1] Griffiths H D and Baker C J 2005 Passive coherent location radar systems: part 1. Performance prediction *IEE Proc., Radar Sonar Navig.* **152** 153–9

[2] Poullin D 2005 Passive detection using digital broadcasters (DAB, DVB) with COFDM modulation *IEE Proc., Radar Sonar Navig.* **152** 143–52

[3] Pollard R 2006 The application of passive radar sensors in ATC *The Institution of Engineering and Technology Seminar on the Future of Civil Radar (Savoy Place, London, UK, June 2006)* (Stevenage, UK: IET) p 55

[4] Griffiths H D and Long N R W 1986 Television-based bistatic radar *IEE Proc., Radar Sonar Navig.* **133** 649–57

[5] Homer J, Kubik K, Mojarrabi B, Longstaff I D, Donskoi E and Cherniakov M 2002 Passive bistatic radar sensing with leos based transmitters *Proc. of IEEE Int. Geoscience and Remote Sensing Symp. (June 2002)* vol 1 pp 438–40

[6] Yarman C E and Yazıcı B 2008 Synthetic aperture hitchhiker imaging *IEEE Trans. Image Process.* **17** 2156–73

[7] Antoniou M, Cherniakov M and Cheng Hu 2009 Space-surface bistatic sar image formation algorithms *IEEE Trans. Geosci. Remote Sens.* **47** 1827–43

[8] Koch V and Westphal R 1995 New approach to a multistatic passive radar sensor for air/space defense *IEEE Aerosp. Electron. Syst. Mag.* **10** 24–32

[9] Cherniakov M, Kubik K and Nezlin D 2000 Bistatic synthetic aperture radar with non-cooperative leos based transmitter *Proc. of IEEE Int. Geoscience and Remote Sensing Symp. (July 2000)* vol 2 pp 861–2

[10] Cherniakov M, Kubik K and Nezlin D 2000 Radar sensors based on communication low earth orbiting satellites microwave emission *Proc. of IEEE Int. Geoscience and Remote Sensing Symp. (July 2000)* vol 3 pp 1007–8

[11] Howland P E, Maksimiuk D and Reitsma G 2005 Fm radio based bistatic radar *IEE Proc., Radar Sonar Navig.* **152** 107–15

[12] Baker C J, Griffiths H D and Papoutsis I 2005 Passive coherent location radar systems: part 2. Waveform properties *IEE Proc., Radar Sonar Navig.* **152** 160–8

[13] Tan D K P, Sun H, Lu Y, Lesturgie M and Chan H L 2005 Passive radar using global system for mobile communication signal: theory, implementation and measurements *IEE Proc., Radar Sonar Navig.* **152** 116–23

[14] He X, Cherniakov M and Zeng T 2005 Signal detectability in ss-bsar with gnss non-cooperative transmitter *IEE Proc., Radar Sonar Navig.* **152** 124–32

[15] Nolan C J and Cheney M 2003 Synthetic aperture inversion for arbitrary flight paths and non-flat topography *IEEE Trans. Image Process.* **12** 1035–43

[16] Barrett H H and Myers K J 2004 *Foundations of Image Science* (Hoboken, NJ: Wiley Interscience)

[17] Treves F 1980 *Introduction to Pseudodifferential and Fourier Integral Operators, vols 1 and 2* (New York: Plenum)

[18] Natterer F and Wübbeling F 2001 *Mathematical Methods in Image Reconstruction* (Philadelphia, PA: SIAM)

[19] Bleistein N and Handelsman R A 1986 *Asymptotic Expansions of Integrals* (New York: Dover)

[20] Grigis A and Sjöstrand J 1994 *Microlocal Analysis for Differential Operators: An Introduction (London Mathematical Society Lecture Note Series* vol 196*)* (Cambridge: Cambridge University Press)

[21] Guillemin V and Sternberg S 1979 *Geometric Asymptotics* (Providence, RI: American Mathematical Society)

[22] Yazici B, Cheney M and Yarman C E 2006 Synthetic-aperture inversion in the presence of noise and clutter *Inverse Problems* **22** 1705–29

[23] Nolan C J and Cheney M 2002 Synthetic aperture inversion *Inverse Problems* **18** 221–36
[24] Quinto E T 1993 Singularities of the x-ray transform and limited data tomography in r^2 and r^3 *SIAM J. Math. Anal.* **24** 1215–25
[25] Wang L, Son I Y and Yazıcı B 2010 Passive imaging using distributed apertures in multiple scattering environments *Inverse Problems* **26** 065002
[26] Son I-Y, Varslot T, Yarman C E, Pezeshki A, Yazici B and Cheney M 2007 Radar detection using sparsely distributed apertures in urban environments *Proc. SPIE on Defense, Security and Sensing* vol 6567, 1Q1–8
[27] Voccola K, Yazici B, Cheney M and Ferrara M 2009 On the equivalence of the generalized likelihood ratio test and backprojection method in synthetic aperture imaging *Proc. SPIE on Defense, Security and Sensing* vol 7335, 1Q1–10
[28] Wang L and Yazıcı B 2010 Passive imaging of moving targets using distributed apertures *Inverse Problems* (submitted)